



Beamspace Channel Estimation for Massive MIMO mmWave Systems: Algorithm and VLSI Design

Journal Article

Author(s):

[Mirfarshbafan, Seyedhadi](#) ; [Gallyas-Sanhueza, Alexandra](#); [Ghods, Ramina](#); [Studer, Christoph](#) 

Publication date:

2020-12

Permanent link:

<https://doi.org/10.3929/ethz-b-000452490>

Rights / license:

[In Copyright - Non-Commercial Use Permitted](#)

Originally published in:

IEEE Transactions on Circuits and Systems I: Regular Papers 67(12), <https://doi.org/10.1109/tcsi.2020.3023023>

Beamspace Channel Estimation for Massive MIMO mmWave Systems: Algorithm and VLSI Design

Seyed Hadi Mirfarshbafan, Alexandra Gallyas-Sanhueza, Ramina Ghods, and Christoph Studer

Abstract—Millimeter-wave (mmWave) communication in combination with massive multiuser multiple-input multiple-output (MU-MIMO) enables high-bandwidth data transmission to multiple users in the same time-frequency resource. The strong path loss of wave propagation at such high frequencies necessitates accurate channel state information to ensure reliable data transmission. We propose a novel channel estimation algorithm called BEAspace CHannel ESTimation (BEACHES), which leverages the fact that wave propagation at mmWave frequencies is predominantly directional. BEACHES adaptively denoises the channel vectors in the beamspace domain using an adaptive shrinkage procedure that relies on Stein’s unbiased risk estimator (SURE). Simulation results for line-of-sight (LoS) and non-LoS mmWave channels reveal that BEACHES performs on par with state-of-the-art channel estimation methods while requiring orders-of-magnitude lower complexity. To demonstrate the effectiveness of BEACHES in practice, we develop a very large-scale integration (VLSI) architecture and provide field-programmable gate array (FPGA) implementation results. Our results show that adaptive channel denoising can be performed at high throughput and in a hardware-friendly manner for massive MU-MIMO mmWave systems with hundreds of antennas.

Index Terms—Millimeter wave (mmWave), massive multiuser MIMO, channel estimation, nonparametric denoising, beamspace, Stein’s unbiased risk estimator (SURE), very large-scale integration (VLSI), field-programmable gate array (FPGA).

I. INTRODUCTION

Millimeter-wave (mmWave) communication [2], [3] and massive multiuser (MU) multiple-input multiple-output (MIMO) [4], [5] are expected to be core technologies of next-generation wireless communication systems. By combining both of these technologies, one can achieve unprecedentedly high-bandwidth data transmission to multiple user equipments (UEs) in the same time-frequency resource via fine-grained beamforming. The strong path loss of wave propagation at

mmWave frequencies necessitates the infrastructure basestations (BSs) to acquire accurate channel state information (CSI) in order to perform data detection in the uplink (UEs transmit to BS) and MU precoding in the downlink (BS transmits to UEs) [6], [7]. To optimally determine the beamforming weights, accurate CSI is not only of paramount importance for hybrid analog-digital BS architectures [8]–[10] but also for emerging all-digital BS architectures [11], [12]. In addition, the trend towards BS architectures with low-precision data converters to reduce power consumption, interconnect bandwidth, and system costs [13]–[15] requires novel algorithms and hardware designs that denoise the estimated channel vectors.

A. Sparsity-Based Channel Estimation

Fortunately, wave propagation at mmWave frequencies is predominantly directional and real-world channels typically comprise only a small number of strong propagation paths, such as a line-of-sight (LoS) component and a few first-order reflections [16]. These properties enable the design of sparsity-exploiting CSI estimation algorithms that effectively suppress channel estimation errors [17]–[20]. Compressive sensing (CS)-based methods have been proposed for mmWave channel estimation in [21], [22], including methods that rely upon orthogonal matching pursuit (OMP) [22]–[24]. The majority of such methods uses a discretization procedure of the number of propagation paths that can be resolved in the *beamspace* (or angular) domain [25], which results in a problem widely known as *basis mismatch* [26]. To avoid the basis mismatch problem, sparse channel estimation for mmWave channels can, for example, be accomplished with atomic norm minimization (ANM) [27], [28] or Newtonized OMP [29]. ANM estimates a discrete set of propagation paths off-the-grid by solving a semidefinite program (SDP). Newtonized OMP (NOMP) is a more efficient alternative to ANM and iteratively refines the incident angles of the dominant propagation paths off-the-grid with a complexity only slightly higher than that of conventional OMP. Although both of these methods do not suffer from the basis mismatch problem and exhibit excellent denoising performance, they entail high computational complexity. Hence, from a hardware-implementation perspective, such methods are less attractive, especially in massive MU-MIMO systems where the complexity is dominated by the large number of BS antennas. In addition, the performance of both of these methods strongly depends on algorithm parameters that need to be tuned for the given propagation conditions.

Another strain of sparsity-exploiting channel-estimation methods build upon approximate message passing (AMP) [30],

S. H. Mirfarshbafan and A. Gallyas-Sanhueza are with the School of Electrical and Computer Engineering at Cornell University, Ithaca, NY, and with Cornell Tech, New York, NY; email: sm2675@cornell.edu, ag753@cornell.edu

R. Ghods was with the School of Electrical and Computer Engineering at Cornell University, Ithaca, NY, and is now with the School of Electrical and Computer Engineering at Carnegie Mellon University, Pittsburgh, PA; email: rghods@cs.cmu.edu

C. Studer was with the School of Electrical and Computer Engineering at Cornell Tech, New York, NY, and Cornell University, Ithaca, NY, and is now with the Department of Information Technology and Electrical Engineering at ETH Zurich, Switzerland. Email: studer@ethz.ch; Web: <http://iis.ee.ethz.ch>

The work of SHM, AGS, and CS was supported in part by Xilinx, Inc. and by ComSenTer, one of six centers in JUMP, a Semiconductor Research Corporation (SRC) program sponsored by DARPA. The work of RG was supported by the US National Science Foundation under grants ECCS-1408006, CCF-1535897, CCF-1652065, CNS-1717559, and ECCS-1824379.

A MATLAB simulator to reproduce the results of this paper is available on GitHub: <https://github.com/IIP-Group/BEACHES-simulator>

A short version of this paper has been presented at the IEEE SPAWC [1].

[31]. While such methods promise high estimation accuracy, they suffer from a number of drawbacks when implemented in VLSI. AMP-based methods require at least two matrix-vector multiplications in each iteration, whose dimension scales with the number of BS antennas, the number of UEs, and the pilot sequence length. In addition, each iteration requires multiple divisions and other nonlinear functions (such as exponentials and Q-functions). As shown in [32], the presence of such nonlinear functions in AMP-based algorithms causes finite-precision issues when implemented with fixed-point arithmetic.

Sparsity has been exploited in many other applications in communication systems, including beam selection in mmWave systems [33], channel estimation for angle-division multiple access [34], and sparse signal recovery via compressive sensing [35]. Even though these results are not directly related to channel estimation in mmWave systems, the proposed adaptive denoising approach might find use in such applications.

B. Contributions

In order to perform denoising-based channel estimation in real-world systems, we propose a low-complexity and adaptive channel estimation algorithm for massive MU-MIMO mmWave systems that can be implemented efficiently in VLSI. Our main contributions are summarized as follows:

- We propose a novel channel estimation algorithm that relies on Stein’s unbiased risk estimator (SURE), which we call BEAmSpace CHannel ESTimation (BEACHES). BEACHES exploits sparsity of mmWave channels in the beamspace domain and adaptively denoises the channel vectors at a fixed computational complexity that scales with $O(B \log(B))$, where B is the number of BS antennas.
- We prove that BEACHES minimizes the mean-square error (MSE) between the noiseless and denoised channel vector in the large-antenna limit, i.e., when $B \rightarrow \infty$, without requiring tedious parameter tuning.
- We evaluate the efficacy of BEACHES for LoS and non-LoS mmWave channel models and show that it performs on par with state-of-the-art channel estimation algorithms in terms of uncoded bit error-rate, but at orders-of-magnitude lower computational complexity.
- We develop a very large-scale integration (VLSI) architecture and present corresponding field-programmable gate array (FPGA) implementation results, which demonstrate that BEACHES enables high-throughput channel estimation in a hardware-efficient manner.

C. Notation

Lowercase and uppercase boldface letters designate column vectors and matrices, respectively. For a vector \mathbf{a} , the k th entry is denoted by $[\mathbf{a}]_k = a_k$; the real and imaginary parts are indicated with $[\mathbf{a}]_{\mathcal{R}} = \mathbf{a}_{\mathcal{R}}$ and $[\mathbf{a}]_{\mathcal{I}} = \mathbf{a}_{\mathcal{I}}$, respectively. The ℓ_1 -norm and ℓ_2 -norm of a vector \mathbf{a} is $\|\mathbf{a}\|_1$ and $\|\mathbf{a}\|_2$, respectively. For a matrix \mathbf{A} , we define its transpose and conjugate transpose as \mathbf{A}^T and \mathbf{A}^H , respectively. The $N \times M$ all-zeros, $N \times N$ identity, and $N \times N$ discrete Fourier transform (DFT) matrices are $\mathbf{0}_{N \times M}$, \mathbf{I}_N , and \mathbf{F} , respectively; the DFT matrix is normalized so that $\mathbf{F}\mathbf{F}^H = \mathbf{I}_N$. Vectors in the

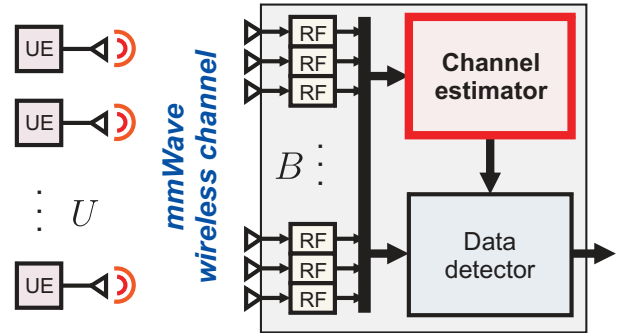


Fig. 1. Considered massive MU-MIMO mmWave uplink system: U user equipments (UEs) transmit pilots over a mmWave wireless channel, which are used to estimate the channel vectors associated to each UE at the B -antenna basestation. This paper focuses on computationally efficient methods that denoise the measured channel vectors in the channel estimator unit.

DFT domain are designated with a hat as in $\hat{\mathbf{a}} = \mathbf{F}\mathbf{a}$. A proper complex-valued Gaussian vector \mathbf{a} with mean vector \mathbf{m} and covariance matrix \mathbf{K} is written as $\mathbf{a} \sim \mathcal{CN}(\mathbf{m}, \mathbf{K})$ and its probability density function (PDF) as $f^{\mathcal{CN}}(\mathbf{a}; \mathbf{m}, \mathbf{K})$. A real-valued Gaussian vector \mathbf{a} with mean vector \mathbf{m} and covariance matrix \mathbf{K} is written as $\mathbf{a} \sim \mathcal{N}(\mathbf{m}, \mathbf{K})$ and its PDF as $f^{\mathcal{N}}(\mathbf{a}; \mathbf{m}, \mathbf{K})$. The expectation operator is $\mathbb{E}[\cdot]$. Optimal values are designated with the superscript $*$.

D. Paper Outline

The rest of the paper is organized as follows. Section II introduces the system model and outlines the concept of denoising-based beamspace channel estimation. Section III details the BEACHES algorithm and presents the simulation results. Section IV proposes a VLSI architecture and provides FPGA implementation results. We conclude in Section V. All proofs are relegated to the appendices.

II. SYSTEM MODEL

We now introduce the system model and summarize existing methods that perform beamspace channel estimation.

A. System Model

We consider a massive MU-MIMO mmWave uplink system as illustrated in Figure 1. The BS is equipped with B antennas arranged as a uniform linear array (ULA) and communicates with U single-antenna UEs in the same time frequency resource.¹ We focus on pilot-based channel estimation, i.e., where the UEs transmit orthogonal pilots in a dedicated training phase and the BS estimates the propagation paths between the UEs and the BS antenna array. Assuming flat-fading channel conditions, the BS estimates the B -dimensional complex channel vector $\mathbf{h} \in \mathbb{C}^B$ for each UE. Furthermore, by assuming that (i) wave propagation is predominantly directional, which is valid if the wavelength is much smaller than the objects interacting with the waves [6], [36], and (ii) the

¹An extension of our algorithm and hardware designs to two-dimensional BS antenna arrays is part of ongoing work.

distance between UE (as well as the scatterers) and BS is sufficiently large, we can use the following well-known plane-wave approximation to model wave propagation at mmWave frequencies from a given UE to the BS [37]:

$$\mathbf{h} = \sum_{\ell=1}^L \alpha_{\ell} \mathbf{a}(\Omega_{\ell}), \quad \mathbf{a}(\Omega) = [e^{j0\Omega}, e^{j1\Omega}, \dots, e^{j(B-1)\Omega}]^T. \quad (1)$$

Here, L refers to the total number of paths arriving at the antenna array (including a potential line-of-sight path), $\alpha_{\ell} \in \mathbb{C}$ is the complex-valued channel gain of the ℓ th path, and $\mathbf{a}(\Omega_{\ell})$ represents a complex-valued sinusoid containing the relative phases between BS antennas, where $\Omega_{\ell} \in [0, 2\pi)$ is determined by the incident angle of the ℓ th path to the antenna array.

With pilot-based channel estimation methods, we only have access to noisy measurements of the channel vector \mathbf{h} . We model such noisy measurements in the antenna domain as

$$\mathbf{y} = \mathbf{h} + \mathbf{e}, \quad (2)$$

where $\mathbf{e} \sim \mathcal{CN}(\mathbf{0}_{B \times 1}, E_0 \mathbf{I}_B)$ represents channel estimation error with variance E_0 per complex entry. Note that for pilot-based channel estimation methods, the channel estimation errors are Gaussian and there is a linear relationship between E_0 and the thermal noise variance N_0 ; see Section III-E for the details.

Remark 1. *The channel model in (1) is appropriate for flat-fading channels assuming UEs with a single transmit antenna. For UEs that are equipped with an antenna array but transmit a single stream (layer) via beamforming, the channel vectors can still be modeled as in (1). For channels that exhibit frequency selectivity, we can consider orthogonal frequency-division multiplexing (OFDM), where each subcarrier is associated with a channel vector as in (1). For single-carrier (SC) transmission in frequency-selective channels or UEs that transmit multiple streams concurrently, multiple channel vectors would need to be estimated (one for each tap in the impulse response and for each layer). An analysis of this scenario is ongoing work. Finally, we emphasize that BEACHES continues to work if the channel vectors follow a more realistic propagation model than the one in (1). The simulation results provided in Section III-E with mmWave channel models confirm this claim.*

Remark 2. *In what follows, we ignore system and hardware impairments, such as timing, frequency, and sampling rate offsets, I/Q imbalance, and analog-to-digital converter (ADC) nonlinearities. In cases where the aggregate effect of the residual hardware impairments can be modeled as Gaussian noise [38], the model in (1) remains valid. For basestation architectures with 1-bit ADCs, a specialized version of BEACHES has been proposed recently in [39]. The design of robust channel estimation algorithms for more specific system and hardware impairments is left for future work.*

B. Beamspace Representation

The model in (1) describes the channel vector in the *antenna domain*, i.e., each entry of the channel vector \mathbf{h} is associated with an antenna element in the BS array. Since the channel vectors \mathbf{h} are modeled as a superposition of L complex-valued sinusoids, it is advantageous to transform the

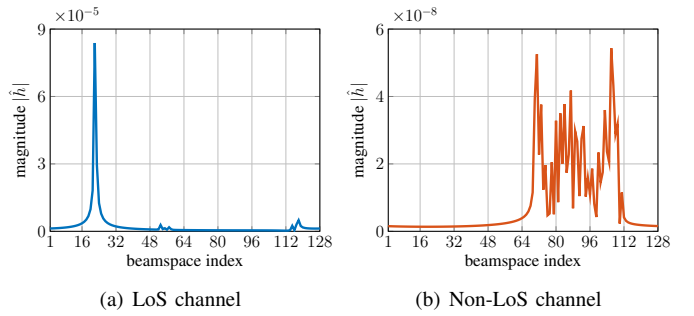


Fig. 2. Examples of a line-of-sight (LoS) channel vector (a) and a non-LoS channel vector (b) in the discrete beamspace domain. The channel vectors are generated with the mmMAGIC UMi model at 60 GHz for a 128 antenna BS with a uniform-linear array (ULA) using $\lambda/2$ antenna spacing. One can clearly see the sparse nature of channel vectors in the beamspace domain.

observed vector \mathbf{y} into the discrete Fourier transform domain according to $\hat{\mathbf{y}} = \mathbf{F}\mathbf{y}$, where \mathbf{F} is the $B \times B$ DFT matrix. This transformation is known to convert the noisy channel vector $\mathbf{y} = \mathbf{h} + \mathbf{e}$ into the so-called *discrete beamspace domain* (also known as angular domain) $\hat{\mathbf{y}}$, in which each entry is associated with a specific incident angle (with respect to the BS antenna array) [25]. More importantly, if the number of paths L is significantly smaller than the number of BS antennas B , then the beamspace representation $\hat{\mathbf{h}}$ of the noiseless channel vector \mathbf{h} will be (approximately) sparse [19]. In other words, most of the channel vector's energy is concentrated on a few entries, which are associated with the indices corresponding to the angles of the arriving waves. This key property of the beamspace representation is illustrated in Figure 2, which shows the magnitude of $\hat{\mathbf{h}}$ for noiseless LoS and non-LoS channel vectors generated with the QuaDRiGa mmMAGIC urban micro (UMi) model at a carrier frequency of 60 GHz [40]. For the LoS case in Figure 2(a), we see that the channel vector consists of one strong LoS component and two weak first-order reflections arriving at two distinct angles.² For the non-LoS case in Figure 2(b), we see that the arriving waves are (i) weaker than for the LoS case and (ii) spread across a wider range of angles. Nevertheless, the channel vector remains to be sparse in the non-LoS case.

C. Channel Vector Denoising in the Beamspace Domain

The sparse nature of mmWave channel vectors in the beamspace domain enables the use of algorithms that denoise the channel vectors at the BS. The main idea behind such channel estimation methods is to first transform the observed noisy channel vector \mathbf{y} in the antenna domain (2) to the beamspace domain according to

$$\hat{\mathbf{y}} = \mathbf{F}\mathbf{y} = \hat{\mathbf{h}} + \hat{\mathbf{e}}, \quad (3)$$

where $\hat{\mathbf{e}} = \mathbf{F}\mathbf{e}$ has the same statistics as the antenna domain channel estimation error vector \mathbf{e} . It is then possible to exploit the fact that most of the arriving signal energy is concentrated

²Note that the strong signal arrived off-the-grid, which causes it to be spread across multiple angular bins. This is an instance of the off-the-grid problem that has been studied extensively in the compressive sensing literature [26].

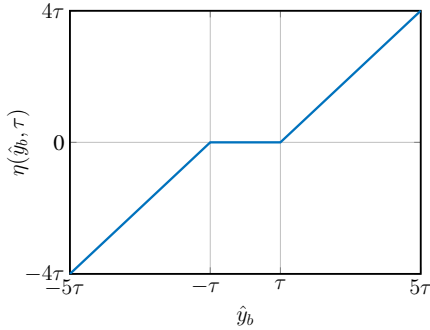


Fig. 3. The soft-thresholding function $\eta(\hat{y}_b, \tau)$ for real values \hat{y}_b .

on a few incident angles and to suppress noise associated with angles that do not pertain to the incoming signals.

To perform denoising, a variety of algorithms have been proposed in the literature (see also the discussion in Section I-A). While most existing methods, such as OMP, suffer from the off-the-grid problem [26], more sophisticated methods such as ANM [27], [28] and NOMP [29], avoid this problem by identifying the dominant paths in the continuous beamspace domain. Unfortunately, such methods exhibit high computational complexity, especially for a large number of BS antennas B , which prevents their use in real-time applications. We next introduce a nonparametric beamspace denoising algorithm that is computationally efficient, can be implemented in hardware, and performs on par with sophisticated off-the-grid beamspace channel estimation algorithms.

III. BEACHES: BEAMSPACE CHANNEL ESTIMATION

We now introduce BEACHES, an efficient algorithm for channel vector denoising in the beamspace domain.

A. Channel Vector Denoising via Soft-Thresholding

The denoising and sparse signal recovery literature [17]–[20], [41] describes a number of algorithms that are suitable for channel-vector denoising in the beamspace domain. The least absolute shrinkage and selection operator (LASSO) [42]–[44] is among the most popular methods, which, in our application, corresponds to the following optimization problem:

$$\eta(\hat{\mathbf{y}}, \tau) = \arg \min_{\hat{\mathbf{h}}' \in \mathbb{C}^B} \frac{1}{2} \|\hat{\mathbf{y}} - \hat{\mathbf{h}}'\|_2^2 + \tau \|\hat{\mathbf{h}}'\|_1. \quad (4)$$

Here, we apply LASSO directly to the beamspace representation of the observed channel vector (3) and $\tau \in \mathbb{R}_+$ is a carefully-chosen denoising parameter. A closed-form expression for the solution to (4) in the complex case has been derived in [45, App. A] and is given by the well-known *soft-thresholding operator* $\eta(\hat{\mathbf{y}}, \tau)$ defined entry-wise as

$$[\eta(\hat{\mathbf{y}}, \tau)]_b = \frac{\hat{y}_b}{|\hat{y}_b|} \max\{|\hat{y}_b| - \tau, 0\}, \quad b = 1, \dots, B, \quad (5)$$

where we define $y/|y| = 0$ for $y = 0$. Figure 3 depicts the soft-thresholding function $\eta(\hat{\mathbf{y}}, \tau)$, which simply shrinks the magnitude of its input by τ or sets it to zero if the magnitude was smaller than τ .

While soft-thresholding is widely used for denoising sparse signals, its performance strongly depends on the choice of the denoising parameter τ [42], [46]. Since the propagation conditions, such as the number of arriving paths (sparsity), the incident angles (locations of the nonzero components), and the received signal strength (magnitudes), can vary widely in wireless communication systems, the design of robust methods that adaptively select the optimal denoising parameter is critical. We now develop an adaptive approach that optimally tunes the denoising parameter τ in a computationally-efficient manner.

Remark 3. *BEACHES only requires knowledge of the noise variance N_0 , which is typically known as it is determined by thermal noise originating in the receiver's RF circuitry.*

B. Computing the Optimal Denoising Parameter

We are interested in computing the optimal denoising parameter τ^* that minimizes the mean square error (MSE) between the denoised beamspace channel vector and the noiseless beamspace channel vector $\hat{\mathbf{h}}$, defined as follows:

$$MSE = \frac{1}{B} \mathbb{E} \left[\|\eta(\hat{\mathbf{y}}, \tau) - \hat{\mathbf{h}}\|_2^2 \right]. \quad (6)$$

In (6), expectation is with respect to $\hat{\mathbf{y}}$. In what follows, we denote the optimal denoised channel vector by $\hat{\mathbf{h}}^* = \eta(\hat{\mathbf{y}}, \tau^*)$.

Unfortunately, determining the optimal denoising parameter τ^* that minimizes the MSE in (6) requires knowledge of the noiseless beamspace channel vector $\hat{\mathbf{h}}$, which is unknown in practice. To resolve this issue, we propose to minimize Stein's unbiased risk estimate (SURE) as a surrogate for the MSE.

The following result provides an expression for SURE in the complex domain and shows that SURE is an unbiased estimator of the MSE that is *independent* of $\hat{\mathbf{h}}$. The proof of the following result is given in Appendix A.

Theorem 1. *Let $\hat{\mathbf{h}} \in \mathbb{C}^B$ be an unknown vector and $\hat{\mathbf{y}} \in \mathbb{C}^B$ a noisy observation vector distributed as $\hat{\mathbf{y}} \sim \mathcal{CN}(\hat{\mathbf{h}}, E_0 \mathbf{I}_B)$. Let $\mu(\hat{\mathbf{y}})$ be an estimator of $\hat{\mathbf{h}}$ from $\hat{\mathbf{y}}$ that is weakly differentiable and operates element-wise on vectors. Then, Stein's unbiased risk estimate given by*

$$SURE = \frac{1}{B} \|\mu(\hat{\mathbf{y}}) - \hat{\mathbf{y}}\|_2^2 + E_0 + \frac{E_0}{B} \sum_{b=1}^B \left(\frac{\partial[\mu_{\mathcal{R}}(\hat{\mathbf{y}})]_b}{\partial[\hat{\mathbf{y}}_{\mathcal{R}}]_b} + \frac{\partial[\mu_{\mathcal{I}}(\hat{\mathbf{y}})]_b}{\partial[\hat{\mathbf{y}}_{\mathcal{I}}]_b} - 2 \right), \quad (7)$$

is an unbiased estimate of the MSE, i.e., satisfies

$$\mathbb{E}[SURE] = MSE. \quad (8)$$

By setting $\mu(\hat{\mathbf{y}}) = \eta(\hat{\mathbf{y}}, \tau)$, we can use Theorem 1 to obtain the following SURE expression for the soft-thresholding function. The proof is given in Appendix B.

Corollary 2. *For the complex-valued soft-thresholding function $\mu(\hat{\mathbf{y}}) = \eta(\hat{\mathbf{y}}, \tau)$ in (5), SURE in (7) is given by³*

$$SURE_\tau = \frac{1}{B} \sum_{b:|\hat{y}_b|<\tau} |\hat{y}_b|^2 + \frac{1}{B} \sum_{b:|\hat{y}_b|>\tau} \tau^2 + E_0$$

³As discussed in Appendix B, the value of $SURE_\tau$ is undefined for $\tau = |\hat{y}_b|$, $b = 1, \dots, B$, due to the non-differentiability of the function $\eta(\hat{\mathbf{y}}, \tau)$.

$$-\frac{E_0}{B}\tau \sum_{b:|\hat{y}_b|>\tau} \frac{1}{|\hat{y}_b|} - \frac{2E_0}{B} \sum_{b:|\hat{y}_b|<\tau} 1. \quad (9)$$

The next result shows that the value of SURE in (9) converges to the MSE given by (6) in the large antenna limit, i.e., for $B \rightarrow \infty$. The proof is given in Appendix C.

Theorem 3. *In the large-antenna limit, where $B \rightarrow \infty$, $SURE_\tau$ in (9) converges to the MSE in (6), i.e., we have*

$$\lim_{B \rightarrow \infty} SURE_\tau = MSE. \quad (10)$$

From Theorems 1 and 3 it is evident that SURE will be an accurate proxy for the MSE in massive MU-MIMO mmWave systems as B is expected to be large. It is crucial to realize that the SURE expression in (9) is *independent* of the true beamspace channel vector $\hat{\mathbf{h}}$. In fact, the result (9) only depends on the magnitudes of the *observed* beamspace channel vector $\hat{\mathbf{y}}$, the channel estimation error variance E_0 (which is determined by the thermal noise variance N_0), the number of BS antennas B , and the denoising parameter τ . This insight combined with the two key properties in (8) and (10) enables us to perform asymptotically-optimal MSE-based denoising by solving the SURE-based quantity

$$\tau^* = \arg \min_{\tau \in \mathbb{R}_+} SURE_\tau. \quad (11)$$

Unfortunately, no closed-form solution to this optimization problem is known. Reference [46] uses a bisection procedure to approximate the optimal value of a similar SURE expression in a sparse signal recovery application. In stark contrast to such approximate methods, we next propose BEACHES, a hardware-friendly algorithm that computes the *optimal* denoising parameter τ^* in (11) using a deterministic procedure whose complexity scales only with $O(B \log(B))$.

Remark 4. *SURE-based denoising was put forward in [42] for wavelet denoising of real-valued signals. In [47], SURE has been applied for denoising complex-valued channel observation in OFDM-based single-antenna systems, exploiting sparsity of the impulse responses. The method in [47] uses SURE to find the coefficients of a frequency-domain filter, while the value of the shrinkage threshold was determined empirically. In contrast to these results, BEACHES exploits sparsity in the beamspace domain and determines the optimal denoising parameter τ^* in $O(B \log(B))$ time. We note that BEACHES could be combined with the method in [47] in order to improve channel estimation in OFDM-based massive MU-MIMO mmWave systems.*

C. The BEACHES Algorithm

Reference [42] outlines an efficient procedure to minimize SURE for wavelet-denoising of real-valued signals. In what follows, we propose a similar strategy to minimize (9) for the complex-valued case. Instead of continuously sweeping the denoising parameter τ through the interval $[0, \infty)$, we first sort the absolute values of the vector $\hat{\mathbf{y}}$ in ascending order and call the resulting sorted vector $\hat{\mathbf{y}}^s$. We then search for the optimal denoising parameter τ only between each pair of consecutive elements of the sorted vector, i.e., $\tau \in (\hat{y}_{k-1}^s, \hat{y}_k^s)$ for $k = 1, \dots, B+1$, where we define $\hat{y}_0^s = 0$ and $\hat{y}_{B+1}^s = \infty$

to account for the first interval $(0, \hat{y}_1^s)$, and last the interval (\hat{y}_B^s, ∞) . In the k th interval, SURE in (9) is a quadratic function of τ given by

$$SURE_{\tau,k} = \frac{1}{B} \underbrace{\sum_{b=1}^{k-1} (\hat{y}_b^s)^2}_{=S} + \frac{(B-k+1)}{B} \tau^2 + E_0 - \frac{E_0}{B} \tau \underbrace{\sum_{b=k}^B (\hat{y}_b^s)^{-1}}_{=V} - \frac{2E_0}{B} (k-1). \quad (12)$$

For each index $k \in \{1, \dots, B+1\}$, we compute the value of $\tau = \tau_k^*$ that locally minimizes $SURE_{\tau,k}$ in the interval $\tau \in (\hat{y}_{k-1}^s, \hat{y}_k^s)$. Since SURE in (12) is a quadratic function of τ , the minimal value in each interval is either at the minimum of the quadratic function (12) or at one of the two interval boundaries⁴, i.e., \hat{y}_{k-1}^s or \hat{y}_k^s . The minimum value of the expression in (12) is attained by $\tau_k^Q = \frac{E_0}{2(B-k+1)} \sum_{b=k}^B (\hat{y}_b^s)^{-1}$. Since the function $SURE_{\tau,k}$ is convex within each interval $(\hat{y}_{k-1}^s, \hat{y}_k^s)$, the optimal parameter τ_k^* in each interval $k = 1, \dots, B+1$, is given by

$$\tau_k^* = \begin{cases} \tau_k^Q, & \hat{y}_{k-1}^s < \tau_k^Q < \hat{y}_k^s, \\ \hat{y}_{k-1}^s, & \tau_k^Q < \hat{y}_{k-1}^s, \\ \hat{y}_k^s, & \tau_k^Q > \hat{y}_k^s, \end{cases} \quad (13)$$

or simply $\tau_k^* = \max\{\hat{y}_{k-1}^s, \min\{\hat{y}_k^s, \tau_k^Q\}\}$. After identifying the optimal value τ_k^* in each interval, the parameter τ^* that achieves the global minimum can be found by comparing all the local minima, i.e., by solving

$$\tau^* = \arg \min_{\tau_k^*, k=1, \dots, B+1} SURE_{\tau_k^*, k}. \quad (14)$$

Our procedure does not need to recalculate SURE in (12) from scratch while searching through $k = 1, \dots, B+1$. Instead, for each value of k , we sequentially update the two quantities $S = \sum_{b=1}^{k-1} (\hat{y}_b^s)^2$ and $V = \sum_{b=k}^B (\hat{y}_b^s)^{-1}$, noting that the magnitudes of the vector $\hat{\mathbf{y}}^s$ are sorted. Algorithm 1, which we call BEACHES, exploits exactly this observation. Lines 5 to 14 detail the search procedure described in (14); this part of the algorithm only involves scalar operations (additions, multiplications, divisions, and comparisons) all of which scale with $O(1)$. As a consequence, this iterative search has a complexity of only $O(B)$. If we assume that the DFT and inverse DFT in line 2 and line 16 are carried out with a fast Fourier transform (FFT) and inverse FFT (IFFT), respectively, and the sorting procedure in line 3 uses a fast sorting algorithm (e.g., merge sort) with complexity $O(B \log(B))$, then the complexity of BEACHES is $O(B \log(B))$. Furthermore, we emphasize that sorting, FFT, iterative scan, and IFFT are all hardware friendly operations; see Section IV for a corresponding VLSI design. A detailed complexity comparison of BEACHES to NOMP and ANM is provided in Section III-F.

⁴Note that $SURE_\tau$ and $SURE_{\tau,k}$ are not defined for $\tau = \hat{y}_{k-1}^s$ and $\tau = \hat{y}_k^s$. We evaluate $SURE_{\tau,k}$ for two values arbitrarily close to these boundaries, i.e., $\tau = \hat{y}_{k-1}^s + \epsilon$ and $\tau = \hat{y}_k^s - \epsilon$ where $\epsilon > 0$ is small compared to τ .

Algorithm 1 BEACHES: BEAmspace CHannel ESTimation

```

1: input  $\mathbf{y}$  and  $E_0$ 
2:  $\hat{\mathbf{y}} = \text{FFT}(\mathbf{y})$ 
3:  $\hat{\mathbf{y}}^s = \text{sort}\{|\hat{\mathbf{y}}|, \text{'ascend'}\}$ ,  $\hat{y}_0^s = 0$ , and  $\hat{y}_{B+1}^s = \infty$ 
4:  $S = 0$ ,  $V = \sum_{k=1}^B (|\hat{y}_k^s|)^{-1}$  and  $\text{SURE}_{\min} = \infty$ 
5: for  $k = 1, \dots, B+1$  do
6:    $\tau_k^* = \max\{\hat{y}_{k-1}^s, \min\{\hat{y}_k^s, \frac{E_0}{2(B-k+1)}V\}\}$ 
7:    $\text{SURE}_{\tau_k^*,k} = \frac{S}{B} + \frac{(B-k+1)}{B}\tau_k^{*2} + E_0$ 
    $\quad - \frac{E_0}{B}\tau_k^*V - \frac{2E_0}{B}(k-1)$ 
8:   if  $\text{SURE}_{\tau_k^*,k} < \text{SURE}_{\min}$  then
9:      $\text{SURE}_{\min} = \text{SURE}_{\tau_k^*,k}$ 
10:     $\tau^* = \tau_k^*$ 
11:   end if
12:    $S = S + (\hat{y}_k^s)^2$ 
13:    $V = V - (\hat{y}_k^s)^{-1}$ 
14: end for
15:  $\hat{h}_k^* = \frac{\hat{y}_k^s}{|\hat{y}_k^s|} \max\{|\hat{y}_k^s| - \tau^*, 0\}$ ,  $k = 1, \dots, B$ 
16:  $\mathbf{h}^* = \text{IFFT}(\hat{\mathbf{h}}^*)$ 
17: return  $\mathbf{h}^*$ 

```

D. Algorithm Simplification for Hardware Implementation

To enable a simpler hardware implementation of BEACHES, which is described in detail in Section IV, we can approximate τ_k^* on line 6 of Algorithm 1 by the value \hat{y}_k^s instead of computing the optimal value τ_k^* exactly. More concretely, we avoid the computations in (13), especially τ_k^Q , and simply use \hat{y}_k^s in the k th iteration, $k = 1, 2, \dots, B$. This approximation is justified by the fact that for large values of B , the gap between any consecutive pair $(\hat{y}_{k-1}^s, \hat{y}_k^s)$ decreases and therefore, the three values \hat{y}_{k-1}^s , \hat{y}_k^s , and τ_k^Q are typically close.⁵ While this approximation helps to reduce the complexity of our hardware implementation, the simulations shown next reveal that the resulting performance is virtually indistinguishable from the original BEACHES algorithm. In addition, we avoid the reciprocal computations $1/B$ on line 7 in Algorithm 1 by scaling the SURE expression by B ; we also omit the constant term E_0 . Both of these tricks do not affect the value of τ^* that minimizes this expression.

E. Simulation Results

To demonstrate the effectiveness of BEACHES, we now present simulation results and a comparison with existing channel vector denoising methods.

1) *Simulated Scenario*: We consider a massive MU-MIMO scenario in which U UEs communicate with a B -antenna BS over $t = 1, \dots, T$ time slots. The input-output relation of the flat-fading system in time slot t is modeled by

$$\mathbf{r}_t = \mathbf{H}\mathbf{s}_t + \mathbf{n}_t. \quad (15)$$

Here, $\mathbf{r}_t \in \mathbb{C}^B$ is the received vector at the BS, $\mathbf{H} \in \mathbb{C}^{B \times U}$ represents the (unknown) MIMO channel, $\mathbf{s}_t = [s_{1,t}, \dots, s_{U,t}]^T$

⁵An alternative approach would be to replace τ_k^* by $\frac{1}{2}(\hat{y}_{k-1}^s + \hat{y}_k^s)$, which results in slightly higher hardware complexity but avoids evaluating SURE at the boundaries. The error-rate and MSE performance of both of these approximations is practically the same as the optimal method.

is the transmit vector with entries chosen from a discrete constellation \mathcal{O} and normalized as $\mathbb{E}[\|\mathbf{s}_t\|_2^2] = \rho^2$, and $\mathbf{n}_t \sim \mathcal{CN}(0, N_0\mathbf{I}_B)$ models thermal noise.

During the channel estimation phase, we sequentially train each column of \mathbf{H} over U time slots. Concretely, in each time slot $t = 1, \dots, U$, one UE is active and transmits $s_{u,t} = \rho$, whereas all others remain inactive. With this training scheme, the estimate of the u th column of the MIMO channel matrix \mathbf{H} can be modeled as $\mathbf{y}_u = \mathbf{h}_u + \mathbf{e}_u$ as done in (2), where the channel estimation error corresponds to $\mathbf{e} \sim \mathcal{CN}(\mathbf{0}, E_0\mathbf{I}_B)$ with variance $E_0 = N_0/\rho^2$ per complex entry. We then perform denoising independently for each column of the noisy observation of \mathbf{H} to obtain an improved channel matrix \mathbf{H}^* .

During the data transmission phase, all UEs $u = 1, \dots, U$ transmit a constellation point from the set \mathcal{O} to the BS concurrently and in the same frequency band; with the same power normalization $\mathbb{E}[\|\mathbf{s}_t\|_2^2] = \rho^2$, as in the training phase. Data detection uses linear minimum-mean-square-error (L-MMSE) equalization [48] with the estimated matrix \mathbf{H}^* .

To characterize the performance of BEACHES and other denoising algorithms, we simulate (i) the uncoded bit error rate for 16-QAM and (ii) the channel estimation MSE as in (6). The channel matrices are generated for both a LoS and a non-LoS conditions using the QuaDRiGa mmMAGIC UMi model [40], at a carrier frequency of 60 GHz with a ULA using $\lambda/2$ antenna spacing. The UEs are placed randomly within a 120° circular sector with minimum and maximum distance of 10 and 110 meters from the BS antenna array, respectively. In addition, we enforce a UE separation of at least 1° (with respect to the BS antenna array) and assume optimal UE power control.

Remark 5. *To enable the readers to perform numerical simulations with other system parameters, channel models, or channel estimation algorithms, our MATLAB simulator is available at <https://github.com/IIP-Group/BEACHES-simulator>*

2) *BER Performance*: Figure 4 shows uncoded bit error rate (BER) simulation results for $B = 128$ BS antennas with $U = 8$ UEs, and $B = 256$ BS antennas with $U = 16$ UEs, for LoS and non-LoS channel conditions.⁶ In addition to BEACHES as detailed in Algorithm 1, we show the BER of the hardware-friendly version described in Section III-D, called “BEACHES (hw)” and that of our fixed-point hardware design called “BEACHES (fp).” We also compare our methods to the following channel estimation methods: (i) Maximum likelihood (ML) channel estimation, (ii) NOMP with software package provided by [29], where we manually tune the false alarm rate P_{fa} for each scenario to optimize performance, (iii) ANM-based denoising, where we use the atomic line spectral estimation toolbox provided by [27] (we use the exact noise variance and the debiased output). As a reference, the results for “exact MSE” use the same soft-thresholding function as in BEACHES, but the optimal denoising parameter τ^* is determined by minimizing the MSE (6), using the noiseless (ground truth) channel vector. Furthermore, “perfect CSI” directly uses the noiseless channel vectors.

⁶The BER at high SNR for the LoS scenario differs slightly to that of our conference paper [1], due to fewer Monte-Carlo trials in that paper.

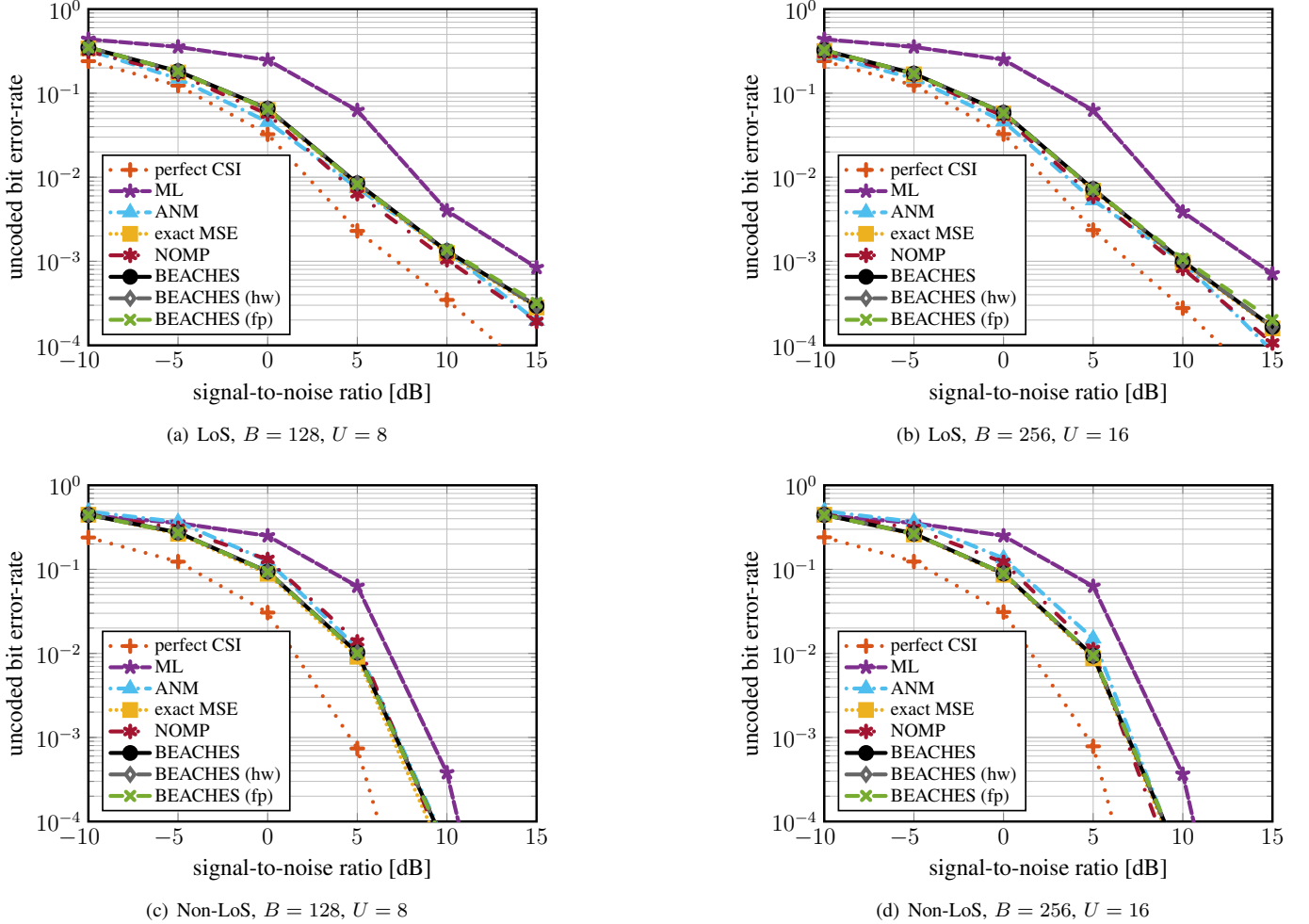


Fig. 4. Uncoded bit error-rate (BER) performance of channel denoising methods for LoS and non-LoS channels. We see that BEACHES performs on par with atomic norm minimization (ANM) and Newtonized OMP (NOMP), and provides 2 dB to 3 dB SNR improvements over ML channel estimation at $BER = 10^{-3}$.

From Figure 4, we see that channel vector denoising in the beamspace domain provides 2 dB to 3 dB SNR performance improvements at $BER = 10^{-3}$ compared to conventional ML channel estimation for the considered scenarios. The performance gains are more pronounced under LoS conditions, but significant error-rate performance improvements are also visible for non-LoS channel conditions. More importantly, we observe that BEACHES performs on par with all other denoising-based channel estimation methods in terms of uncoded BER for the considered scenarios. This observation indicates that off-the-grid denoising methods, such as NOMP and ANM, do not provide a critical performance advantage over BEACHES. Furthermore, our hardware friendly algorithm “BEACHES (hw)” and the fixed-point version “BEACHES (fp)” deliver the same performance as BEACHES.

3) *MSE Performance*: Figure 5 shows the MSE of channel estimation for the same scenarios and algorithms considered in Figure 4. In terms of MSE, the performance of ANM and NOMP is superior to that of BEACHES for LoS channels. We address this to the fact that the channel realizations are extremely sparse under such conditions (cf. Figure 2(a)). For non-LoS channels, all methods perform equally well.

We address this observation to the fact that the beamspace representation for these non-LoS channels is not sufficiently sparse (cf. Figure 2(b)) to leverage the off-the-grid capabilities provided by ANM and NOMP. These simulations also indicate that the MSE is not a particularly reliable metric to predict the BER performance of channel estimation methods in massive MU-MIMO mmWave systems.

F. Complexity Scaling and Runtime Comparison

We now compare the complexity scaling of BEACHES to that of NOMP and ANM. We furthermore provide a MATLAB runtime comparison for LoS and non-LoS channels. In what follows, we assume that the complexity of a $B \times B$ matrix inversion and eigenvalue decomposition scales with $O(B^3)$.

1) *Complexity Scaling*: As mentioned in Section III-C, the complexity of BEACHES scales with $O(B \log(B))$ and is dominated by the FFT, IFFT, and sorting operations.

The complexity of NOMP scales with [29]

$$O(K\gamma B \log(\gamma B) + K^2 B + BK^3 + K^4), \quad (16)$$

where γ is the frequency oversampling factor (typically set to 4) and K represents the number of NOMP iterations, which also

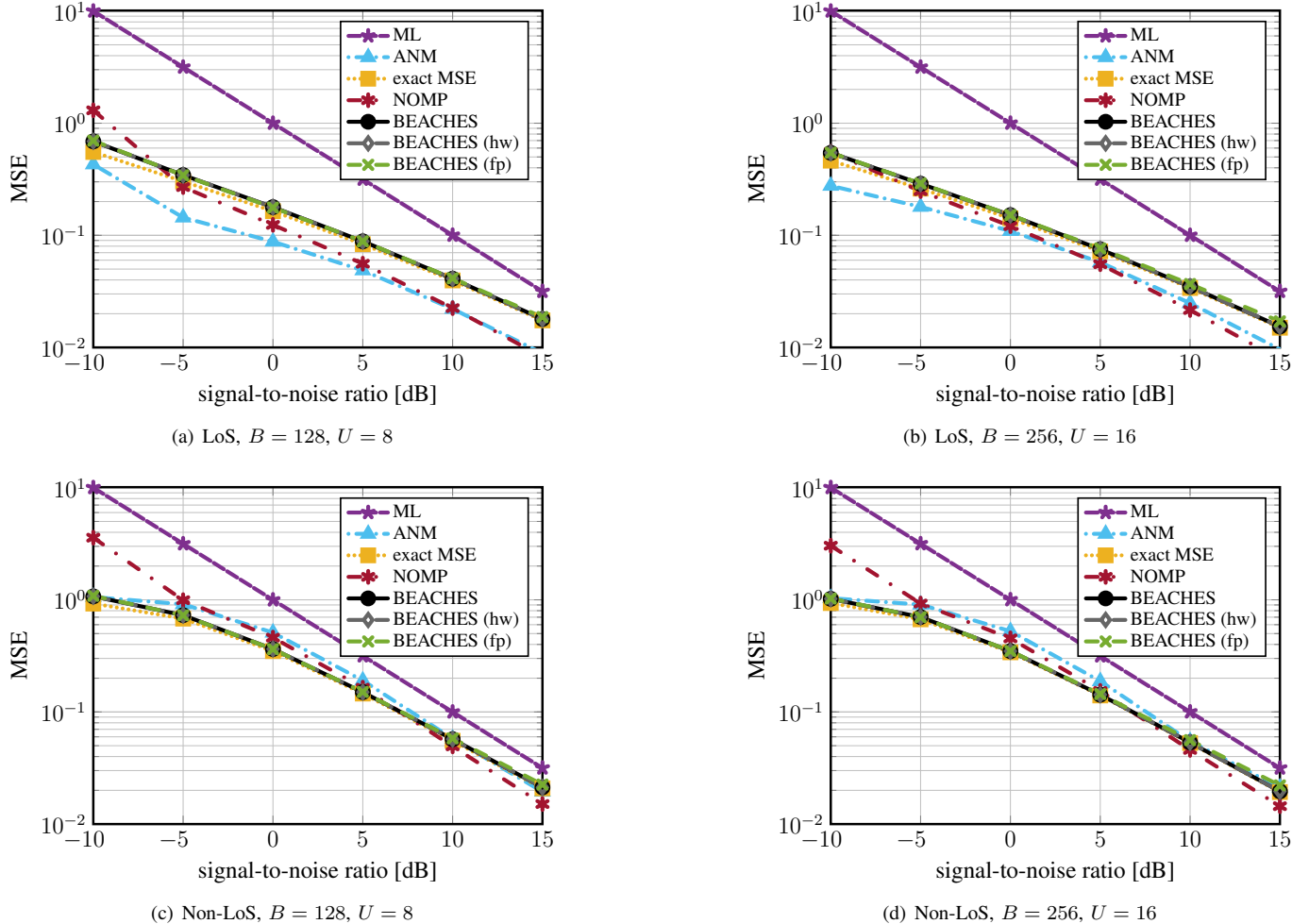


Fig. 5. Mean-square error (MSE) performance of channel denoising methods for LoS and non-LoS channels. We see that BEACHES provides 2.5 \times to 6 \times MSE improvement over ML channel estimation at $SNR = 0$ dB.

specifies the number of detected complex sinusoids. The exact value of K is determined internally by NOMP and depends on a number of factors, including the false alarm rate P_{fa} , the SNR, and the channel scenario, all of which affect the sparsity level of the observation vector. We have observed typical values for K ranging from 2 to 45 for the simulated scenarios in Section III-E. For large B , the complexity of NOMP is dominated by the term $K\gamma B \log(\gamma B)$ in (16). Hence, by ignoring the term BK^3 in (16), the complexity of NOMP is at least $K\gamma/3$ times higher than that of BEACHES—we confirm this observation in the runtime comparison of Section III-F2.

The complexity of ANM scales with $O(K'B^3)$, where K' is the number of iterations of the fast alternating direction method of multipliers (ADMM) implementation provided by [27]. Each algorithm iteration requires a projection onto the semidefinite cone, which can be implemented via an eigenvalue decomposition whose complexity scales with $O(B^3)$ [49]. We have observed typical values of K' ranging from 130 to 360 for the simulated scenarios in Section III-E. Consequently, ANM has orders-of-magnitude higher complexity than BEACHES, especially for a large number of BS antennas B —we confirm this observation by the runtime comparison detailed next.

TABLE I
MATLAB RUNTIMES IN MILLISECONDS (AND NORMALIZED RUNTIMES) ON AN INTEL CORE I5-7400 CPU WITH 16 GB RAM.

Scenario	BEACHES	NOMP	ANM
$B = 128$, LoS	0.57 (1 \times)	28.36 (50 \times)	5221 (9100 \times)
$B = 128$, non-LoS	0.40 (1 \times)	260.4 (650 \times)	7725 (19000 \times)
$B = 256$, LoS	1.64 (1 \times)	199.9 (120 \times)	47968 (29000 \times)
$B = 256$, non-LoS	1.45 (1 \times)	2204 (1500 \times)	83750 (58000 \times)

2) *Runtime Comparison:* While the performance in terms of uncoded BER is comparable for all considered channel estimation methods, BEACHES exhibits (often significantly) lower complexity than NOMP and ANM. To reinforce this claim, we measured their MATLAB runtimes in milliseconds on an Intel core i5-7400 CPU with 16 GB RAM at a signal-to-noise ratio (SNR) of 5 dB; at higher SNRs, the runtimes of NOMP and ANM increase by up to 2 \times whereas the runtime of BEACHES remains unaffected. Table I demonstrates that the runtime of BEACHES is orders-of-magnitude lower than that of NOMP (up to 1500 \times) and ANM (up to 58000 \times), while the speedup is more pronounced for $B = 256$ BS antennas

than for $B = 128$ BS antennas.

Remark 6. *MATLAB runtime measurements can only serve as a proxy to the true complexity as they hide the effect of coding details. Nevertheless, the extreme speedups for channel vector denoising shown in Table I confirm the inherent complexity advantages of BEACHES over ANM and NOMP reflected in our analytical expressions provided in Section III-F1.*

Remark 7. *The complexity scaling analysis and runtime comparison in Table I hides an important aspect: NOMP and ANM can be used for compressive channel estimation whereas BEACHES can only be used for beamspace channel vector denoising. The development of efficient off-the-grid channel estimation methods specialized to beamspace channel vector denoising is an interesting open research problem.*

IV. VLSI DESIGN AND FPGA IMPLEMENTATION

We now describe a VLSI architecture of the simplified version of BEACHES described in Section III-D, and present reference FPGA implementation results.

A. Architecture Overview

Figure 6 provides a high-level overview of the proposed VLSI architecture that implements the hardware (hw) version of BEACHES presented in Section III-D. The architecture consists of three main modules: (i) an antenna-to-beamspace (A2B) conversion module, (ii) a SURE-based denoiser (SBD) module, and (iii) a beamspace-to-antenna (B2A) conversion module. The A2B module transforms the received antenna-domain channel vector \mathbf{y} into the beamspace domain vector $\hat{\mathbf{y}}$ as given by (3). The same module also converts the individual entries of the vector $\hat{\mathbf{y}}$ from Cartesian coordinates to polar coordinates, which simplifies the adaptive denoising procedure. The SBD module implements SURE-based denoising, i.e., first identifies the optimal denoising parameter τ^* and then applies the shrinkage to the magnitudes of the beamspace vector entries \hat{y}_k , $k = 1, \dots, B$. The B2A module converts the entries of the denoised beamspace vector \hat{h}_k^* , $k = 1, \dots, B$, from polar into Cartesian coordinates. The same module also transforms the denoised beamspace vector $\hat{\mathbf{h}}^*$ back into the antenna domain \mathbf{h}^* . To maximize throughput, the proposed architecture relies on input/output streaming. Concretely, the architecture reads a new channel vector entry and generates a new denoised entry (after a certain processing latency) in each clock cycle. The streaming nature of the proposed architecture also reduces control overhead and the need for additional storage of intermediate results.

B. Architecture Details

The architecture details of the three modules shown in Figure 6 are as follows.

1) *Antenna-to-Beamspace (A2B) Conversion Module:* As shown in Figure 6, the A2B conversion module contains a streaming FFT that transforms the noisy antenna-domain channel vector into the beamspace domain. In our implementation, we use a Xilinx LogiCORE FFT IP with radix-2 pipelined

I/O streaming, which reads and generates one vector entry per clock cycle. As a consequence, the FFT core completes computation of the $B \times 1$ beamspace vector $\hat{\mathbf{y}}$ every B clock cycles. To reduce area, we configured the FFT core to scale down the intermediate values by a factor of two in each of the $\log_2(B)$ FFT stages. This configuration reduces the dynamic range in each FFT stage and also reduces resource utilization. Additionally, this scaling approach yields FFT outputs that have smaller dynamic range compared to the unscaled case, which allows for more compact fixed-point data representation and reduces storage requirements in the subsequent modules.

After FFT processing, each complex-valued beamspace domain sample \hat{y}_k is passed through a vectoring CORDIC, which converts the Cartesian number representation into polar coordinates. This transform simplifies the soft-thresholding operation, as it only needs to be applied to the magnitude of each entry in the SBD module—the phase remains untouched. The CORDIC is implemented using a Xilinx LogiCORE IP. The number of microrotations in the CORDIC core is determined by the IP so that the achieved accuracy is 10 bit; see Section IV-C for more details on the fixed-point parameters of our design.

2) *SURE-based Denoiser (SBD) Module:* As shown in Figure 6, this module consists of a first-in first-out (FIFO) buffer, a module to perform sort-and-scan (SAS) in order to determine the optimal denoising threshold, and logic (a subtractor and a multiplexer) to apply soft-thresholding to the values in the FIFO buffer. The role of the FIFO buffer is to delay the inputs of the SBD module so that they are ready as soon as the optimal threshold τ^* has been computed. The FIFO buffer has a depth of $2B + 5$ entries, corresponding to the latency of the SAS submodule as detailed in the next paragraphs. The details of the SAS architecture are shown in Figure 7. The architecture consists of a sort unit and a subsequent scan unit, corresponding to lines 3 to 14 of Algorithm 1. The following paragraphs summarize the most important architecture details.

As depicted in Figure 7, the sort unit consists of an array of B identical processing elements (PEs). The details of the PEs are shown for the second PE (PE-2), which consists of (i) a register to keep one of the sorted elements, (ii) a multiplexer that selects whether the new input data or the value stored in the previous PE should enter the register, (iii) a comparator (denoted by “cmp”) that compares the new input value with the value stored in the PE’s register, and (iv) a control unit (denoted by “ctrl”) that determines the multiplexer output and whether the register must be updated. As for the FFT core, the sort unit is using I/O streaming, i.e., the architecture continuously reads and generates data. This architecture also allows for a seamless integration with the scan unit (discussed below), and eliminates the need to buffer the sorted data separately in a memory for the scan unit to work on. The sort unit sorts the data as they enter, by finding the appropriate position within the array for each new input data, similar to an insertion sort algorithm. Assume that k entries of a $B \times 1$ vector have already been sorted and reside in the PEs 1 to k . In the next clock cycle, the $(k+1)$ th (unsorted) element enters the sort unit and is broadcast to all PEs. Each PE compares the new element with the value stored in its own register, and additionally, receives the result of the same comparison from its preceding PE. For the case

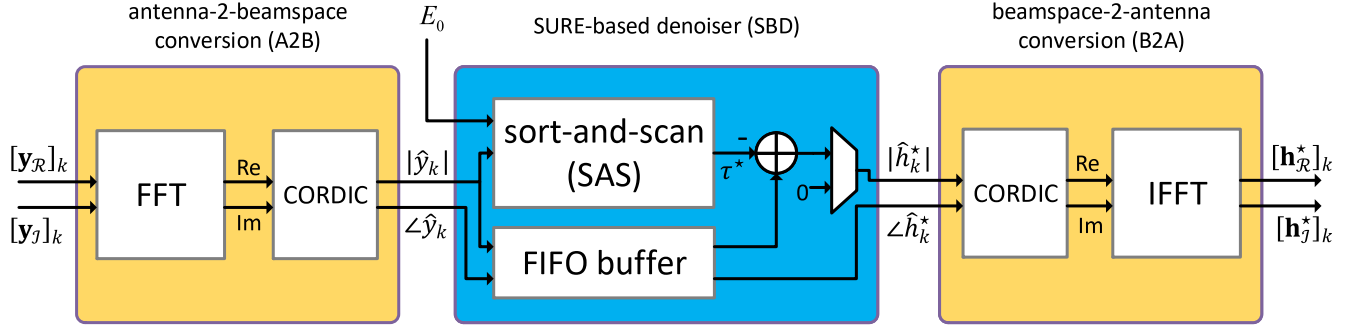


Fig. 6. High-level VLSI architecture of BEACHES (hw). The architecture operates in input/output streaming mode and consists of three modules: an antenna-to-beamspace (A2B) conversion module, a SURE-based denoiser (SBD) module, and a beamspace-to-antenna (B2A) conversion module. The only required parameter is the variance E_0 of the channel estimation noise, which is known in practical systems.

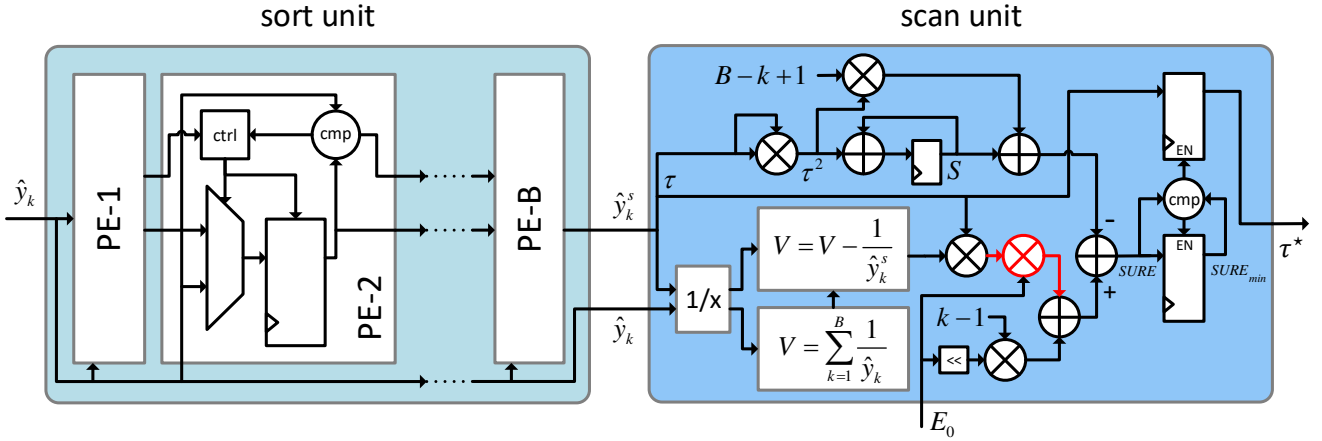


Fig. 7. Architecture details of the sort-and-scan (SAS) module that supports I/O streaming. The sort unit (left) sorts the magnitudes of the beamspace vector in descending order (PE- B contains the smallest sorted element) using a linear array of comparators; the scan unit uses the sorted outputs to determine the optimal SURE threshold τ^* for shrinkage-based denoising. The critical path of this architecture is in the scan unit and highlighted with red color.

of sorting in descending order (i.e., PE- B stores the smallest element), the new input data will be placed in PE- m , if the new element is larger than the data stored in PEs $1, \dots, m-1$ and smaller than or equal to the value stored in PE- m . At the same time, the PEs m, \dots, k will pass their previously stored values to their adjacent PE (e.g., PE- m to PE- $(m+1)$), so that no data is lost. This approach is repeated until all B elements are sorted in all of the PEs at the clock cycle after receiving the last element. When loading the first element of the next denoising problem, PE- B will pass its value (which is the smallest element of the last channel vector) to the scan unit and will receive the data of PE- $(B-1)$, and therefore the sorted data will be flushed at the same time the next problem is being loaded and sorted.

Remark 8. *Although the algorithm complexity of BEACHES is $O(B \log(B))$, the implemented sorting architecture has a hardware complexity of $O(B^2)$ in terms of the area-delay product. The reason for this architecture choice is the fact that this sorting method supports I/O streaming without a significant overhead in terms of latency and buffering. Furthermore, our implementation results in Section IV-D demonstrate that this architecture is efficient for the targeted BS antenna numbers.*

The scan unit is depicted in Figure 7. In order to initialize

the cumulative sum of reciprocals denoted by V on line 4 of Algorithm 1, the scan unit receives the entries of $\hat{\mathbf{y}}$ at the same time they enter the sort unit. The reciprocal values of the entries of $\hat{\mathbf{y}}$ are computed sequentially using a look-up-table (LUT) with 512 entries and are accumulated in a register. Therefore, the cumulative sum of reciprocals is ready once the scan unit receives the the last element of $\hat{\mathbf{y}}$. At the same time, the first sorted entry of $\hat{\mathbf{y}}$ comes out of the sort unit. As the scan unit receives the sorted elements \hat{y}_k^s , it updates the value of the quantity V according to the line 13 of Algorithm 1. The rest of the scan unit contains adders/subtractors and multipliers to compute SURE corresponding to line 7 of the Algorithm 1 (with modifications detailed in Section III-D). Finally, the registers and the comparator at the right end of the scan unit in Figure 7, implement the conditional assignments corresponding to the lines 8 to 11 of the algorithm.

The critical path of the proposed BEACHES architecture is in the scan unit as indicated with red color in Figure 7. The critical path originates in a pipeline flip-flop, goes through a real-valued multiplier, and ends in another pipeline flip-flop. For the sake of simplicity, the pipeline registers are not shown.

3) *Beamspace-to-Antenna (B2A) Conversion Module:* As shown in Figure 6, the B2A conversion module resembles that of the A2B module. This module contains a rotation

CORDIC, implemented by Xilinx LogiCORE IP, to transform the denoised entries from polar into Cartesian coordinates, and a Xilinx LogiCORE FFT IP to convert the denoised beamspace entries into the antenna domain. The FFT core is configured to perform an IFFT without scaling in any of its stages. The unscaled configuration results in a word-length growth in every stage. However, since the beamspace domain signals are already scaled by the FFT core in the A2B module, the same word-length as the input channel entries is sufficient to accommodate the dynamic range of the outputs from the unscaled IFFT.

C. Fixed-Point Parameters

To maximize hardware-efficiency, we use two's complement fixed-point arithmetic. The number of bits used for signals in our implementation has been determined based on extensive bit error-rate (BER) simulations, with the goal of achieving near-floating-point performance while minimizing area. For the antenna domain channel entries, we use 16 bits of which are 8 fractional bits. Due to the FFT scaling described in Section IV-B1, 10 bits are sufficient for the beamspace vector entries. Therefore, the entries of the vectors $\hat{\mathbf{y}}$ and $\hat{\mathbf{y}}^*$ are represented with 10 bits of which are 8 fractional bits, in both the Cartesian and polar coordinates. Since the SBD module (shown in Figure 6) operates in the beamspace domain, most of its signals are represented with 10-bit numbers. For the quantity E_0/B , we use 16-bit numbers with 15 fraction bits. We have eliminated the term E_0 in line 8 of Algorithm 1, since it is a constant and does not affect the value of the optimal threshold. For the entries of the LUT which is used to compute reciprocals in the scan unit, we use 12-bit numbers with 2 fraction bits. Other intermediate signals in the scan unit have customized word-lengths to accommodate temporary dynamic range growth caused by multiplications and additions.

The BER and MSE performance of our fixed-point BEACHES architecture are shown in Figure 4 and Figure 5, respectively, where “fp” stands for fixed-point performance. Clearly, the loss due to finite-precision arithmetic is negligible compared to the reference floating-point MATLAB model.

D. FPGA Implementation Results

To demonstrate the efficacy of BEACHES in practice, we have implemented our architecture on a Xilinx Virtex-7 XC7VX690T FPGA (speed grade -3) for various BS antenna configurations ($B = 64, 128, 256, 512$). The implementation results are summarized in Table II, and confirm the low complexity of BEACHES when implemented in hardware. In fact, the resource utilization (in terms of slices, LUTs, flip-flops, DSP48 units, and block RAMs) is within a few percent of the total FPGA resources. Furthermore, we observe that the resource utilization (measured in terms of LUTs and flip-flops) increase roughly linearly with the number of BS antennas, which is mainly due to the fact that the number of comparison PEs in the SAS module grows linearly in B . Similarly, we see that the throughput (measured in million vectors denoised per second) decreases roughly linearly in B . The hardware efficiency (measured in million entries per LUT) also reduces approximately linearly in B , which is intuitive as more work

must be carried out by BEACHES for systems with more BS antennas. Table III shows a detailed area breakdown of our FPGA designs. We can see that for $B = 64$, the three modules (A2B, SBD, and B2A) occupy about the same amount of resources. However, when increasing B , we see that the complexity of the SBD unit dominates. This is due to the fact that the complexity of the sorting module is the only one whose resources grow linearly in B . Evidently, if one is interested in further increasing the number of BS antennas B , alternative sorting engines should be used.

Remark 9. *The BEACHES design supporting $B = 512$ BS antennas, which achieves the lowest throughput in Table II, denoises up to 570 000 channel vectors per second. By assuming a system with $U = 16$ UEs, this architecture can denoise up to 35 625 channel matrices per second, i.e., one channel matrix every 28 μ s. Since typical coherence times of mmWave channels are in the order of several milliseconds [50], channels need to be estimated roughly once every 1000 μ s. Therefore, the throughput of our FPGA designs are well above what is required for mmWave channel estimation.*

We conclude by noting that there exists, to the best of our knowledge, no channel vector denoising implementation in the open literature that would enable a fair comparison. Nevertheless, a handful of results in the literature are concerned with hardware designs for sparsity-based channel estimation algorithms, such as [23], [51], [52]. The hardware designs reported in [23] are for wideband single-input single-output (SISO) channels in 3GPP-LTE systems. These implementations exploit sparsity in the delay domain and are based on three serial greedy pursuit algorithms, namely matching pursuit, gradient pursuit, and OMP. The FPGA design reported in [51] focuses on channel estimation of indoor SISO systems—again, this result exploits sparsity in the delay domain. The results in [52] focus on short-range, point-to-point, indoor communication with hybrid precoding—a direct comparison of these methods to our work is difficult. We reiterate that all these results do not focus on massive MU-MIMO mmWave denoising in the beamspace domain and require the user to set certain algorithm parameters. In contrast, BEACHES is specialized to perform adaptive denoising in the beamspace domain while only requiring knowledge of the noise variance.

V. CONCLUSIONS

We have proposed a nonparametric channel estimation algorithm for massive MU-MIMO mmWave systems, which we call BEAmSpace CHannel ESTimation (BEACHES). BEACHES exploits channel sparsity of mmWave channels in the beamspace domain in order to perform adaptive denoising via Stein's unbiased risk estimate (SURE). We have established that BEACHES achieves MSE-optimal performance in the large-antenna limit. For realistic LoS and non-LoS mmWave channel models, we have shown that BEACHES performs on par with sophisticated channel estimation algorithms in terms of uncoded bit-rate performance but at orders-of-magnitude lower complexity. As a direct consequence of the nonparametric nature of our algorithm, BEACHES continues to minimize the

TABLE II
IMPLEMENTATION RESULTS FOR DIFFERENT NUMBERS OF BS ANTENNAS B ON A XILINX VIRTEX-7 XC7VX690T FPGA.

BS antennas B	64	128	256	512
Slices	1 532 (1.41%)	2099 (1.94%)	3 089 (2.85%)	4 886 (4.51%)
LUTs	4 564 (1.05%)	6 391 (1.48%)	9 394 (2.17%)	14 449 (3.34%)
– logic LUTs	3 970 (0.92%)	5 566 (1.28%)	8 336 (1.92%)	13 523 (3.12%)
– memory LUTs	594 (0.34%)	825 (0.47%)	1 058 (0.61%)	926 (0.53%)
Flipflops	5 561 (0.64%)	7 015 (0.81%)	9 282 (1.07%)	13 133 (1.52%)
DSP48 units	24 (0.67%)	32 (0.89%)	32 (0.89%)	40 (1.11%)
Block RAMs	1 (0.07%)	1 (0.07%)	2 (0.14%)	5.5 (0.37%)
Max. clock frequency [MHz]	303	303	303	294
Latency [clock cycles]	575	972	1752	3301
Latency [μ s]	1.8	3.2	5.8	10.9
Throughput ^a [Mvectors/s]	4.73	2.36	1.18	0.57
Power consumption ^b [W]	0.76	0.87	0.98	1.29
Efficiency [Mentries/s/LUT]	66 389	47 410	32 255	20 970

^aThe throughput is given in million vectors denoised per second and calculated as f/B , where f is the maximum clock frequency.

^bStatistical power estimation at maximum clock frequency and for 1.0V supply voltage.

TABLE III
FPGA RESOURCE AND LATENCY BREAKDOWN FOR DIFFERENT NUMBERS OF BS ANTENNAS B ON A XILINX VIRTEX-7 XC7VX690T FPGA.

BS antennas B	64			128			256			512		
	A2B	SBD	B2A	A2B	SBD	B2A	A2B	SBD	B2A	A2B	SBD	B2A
LUTs	1 650	1 517	1 408	1 947	2 798	1 658	2 176	5 331	1 899	2 381	9 985	2 092
– logic LUTs	1 354	1 450	1 177	1 542	2 691	1 345	1 701	5 144	1 503	1 885	9 978	1 669
– memory LUTs	296	67	231	405	107	313	475	187	396	496	7	423
Flipflops	2 470	994	2 097	2 834	1 769	2 412	3 190	3 312	2 780	3 646	6 374	3 113
DSP48 units	9	5	10	13	5	14	13	5	14	17	5	18
Latency [clock cycles]	218	136	221	353	264	355	615	520	617	1134	1032	1135

channel estimation MSE even in scenarios where no sparsity can be exploited (e.g., for Rayleigh fading channels).

In order to demonstrate the practicality of BEACHES, we have developed reference FPGA implementations for massive MU-MIMO mmWave systems with hundreds of BS antennas. Our results are a proof-of-concept that high-quality mmWave channel estimation can be performed at high throughput and in a hardware-efficient manner.

There are many avenues for future work. An adaptation of BEACHES to single-carrier (SC) transmission in mmWave channels is a challenging open research problem. The development of nonparametric channel estimation methods that do not need knowledge of the noise variance is part of ongoing work. An extension of BEACHES to basestation architectures that use decentralized baseband processing [53] to reduce interconnect bottlenecks is an interesting open research problem. Finally, alternative sorting architectures might be necessary when targeting systems with thousands of antenna elements.

ACKNOWLEDGMENTS

The authors thank O. Castañeda for his help during the FPGA design, C. Jeon for discussions on SURE-based denoising, and D. Stiverson for his preliminary exploration of low-complexity beamspace channel estimation algorithms for mmWave systems.

APPENDIX A PROOF OF THEOREM 1

We first derive the general form for SURE with complex-valued signals. The MSE for a weakly-differentiable estimator function $\mu(\hat{\mathbf{y}})$ is defined as

$$MSE = \frac{1}{B} \mathbb{E} \left[\|\mu(\hat{\mathbf{y}}) - \hat{\mathbf{h}}\|_2^2 \right]. \quad (17)$$

Note that expectation is with respect to the noisy observation $\hat{\mathbf{y}}$. We decompose the complex-valued vector $\hat{\mathbf{y}}$ into the real part $\hat{\mathbf{y}}_{\mathcal{R}} \sim \mathcal{N}(\mathbf{y}_{\mathcal{R}}; \hat{\mathbf{h}}_{\mathcal{R}}, \frac{E_0}{2} \mathbf{I}_B)$ and imaginary part $\hat{\mathbf{y}}_{\mathcal{I}} \sim \mathcal{N}(\mathbf{y}_{\mathcal{I}}; \hat{\mathbf{h}}_{\mathcal{I}}, \frac{E_0}{2} \mathbf{I}_B)$ and define $g(\hat{\mathbf{y}}) = \mu(\hat{\mathbf{y}}) - \hat{\mathbf{y}}$. Hence,

$$MSE = \frac{1}{B} \mathbb{E} \left[\|g(\hat{\mathbf{y}}) + \hat{\mathbf{y}} - \hat{\mathbf{h}}\|_2^2 \right] \quad (18)$$

$$= \frac{1}{B} \mathbb{E} \left[\|g(\hat{\mathbf{y}})\|_2^2 \right] + \frac{1}{B} \mathbb{E} \left[\|\hat{\mathbf{y}} - \hat{\mathbf{h}}\|_2^2 \right] \\ + \frac{1}{B} \mathbb{E} \left[2 \left[g(\hat{\mathbf{y}})^{\text{H}} (\hat{\mathbf{y}} - \hat{\mathbf{h}}) \right]_{\mathcal{R}} \right]. \quad (19)$$

The last term can be expanded as follows:

$$\frac{2}{B} \mathbb{E} \left[\left[g(\hat{\mathbf{y}})^{\text{H}} (\hat{\mathbf{y}} - \hat{\mathbf{h}}) \right]_{\mathcal{R}} \right] \quad (20) \\ = \frac{2}{B} \mathbb{E} \left[g_{\mathcal{R}}(\hat{\mathbf{y}})^{\text{T}} (\hat{\mathbf{y}}_{\mathcal{R}} - \hat{\mathbf{h}}_{\mathcal{R}}) \right] + \frac{2}{B} \mathbb{E} \left[g_{\mathcal{I}}(\hat{\mathbf{y}})^{\text{T}} (\hat{\mathbf{y}}_{\mathcal{I}} - \hat{\mathbf{h}}_{\mathcal{I}}) \right].$$

We can now expand $\frac{2}{B} \mathbb{E} \left[g_{\mathcal{R}}(\hat{\mathbf{y}})^{\text{T}} (\hat{\mathbf{y}}_{\mathcal{R}} - \hat{\mathbf{h}}_{\mathcal{R}}) \right]$, which yields

$$\frac{2}{B} \mathbb{E} \left[g_{\mathcal{R}}(\hat{\mathbf{y}})^{\text{T}} (\hat{\mathbf{y}}_{\mathcal{R}} - \hat{\mathbf{h}}_{\mathcal{R}}) \right]$$

$$= \frac{2}{B} \int_{\hat{\mathbf{y}}} f^{\mathcal{CN}} \left(\hat{\mathbf{y}}; \hat{\mathbf{h}}, E_0 \mathbf{I}_B \right) \sum_{b=1}^B [g_{\mathcal{R}}(\hat{\mathbf{y}})]_b \times \quad = 1 - \tau \frac{[\hat{\mathbf{y}}_{\mathcal{R}}]_b^2}{([\hat{\mathbf{y}}_{\mathcal{R}}]_b^2 + [\hat{\mathbf{y}}_{\mathcal{I}}]_b^2)^{3/2}}. \quad (32)$$

$$([\hat{\mathbf{y}}_{\mathcal{R}}]_b - [\hat{\mathbf{h}}_{\mathcal{R}}]_b) d\hat{\mathbf{y}} \quad (21)$$

$$= \frac{2}{B} \int_{\hat{\mathbf{y}}_{\mathcal{I}}} f^{\mathcal{N}} \left(\hat{\mathbf{y}}_{\mathcal{I}}; \hat{\mathbf{h}}_{\mathcal{I}}, \frac{E_0}{2} \mathbf{I}_B \right) \sum_{b=1}^B \int_{[\hat{\mathbf{y}}_{\mathcal{R}}]_b} \frac{1}{(2\pi \frac{E_0}{2})^{B/2}} \times \quad (22)$$

$$([\hat{\mathbf{y}}_{\mathcal{R}}]_b - [\hat{\mathbf{h}}_{\mathcal{R}}]_b) d[\hat{\mathbf{y}}_{\mathcal{R}}]_b d\hat{\mathbf{y}}_{\mathcal{I}}$$

$$\stackrel{(a)}{=} \frac{2}{B} \int_{\hat{\mathbf{y}}_{\mathcal{I}}} f^{\mathcal{N}} \left(\hat{\mathbf{y}}_{\mathcal{I}}; \hat{\mathbf{h}}_{\mathcal{I}}, \frac{E_0}{2} \mathbf{I}_B \right) \sum_{b=1}^B \int_{[\hat{\mathbf{y}}_{\mathcal{R}}]_b} \frac{1}{(2\pi \frac{E_0}{2})^{B/2}} \times \quad (23)$$

$$\exp \left(-\frac{([\hat{\mathbf{y}}_{\mathcal{R}}]_b - [\hat{\mathbf{h}}_{\mathcal{R}}]_b)^2}{2 \frac{E_0}{2}} \right) [g_{\mathcal{R}}(\hat{\mathbf{y}})]_b \times$$

$$= \frac{2}{B} \int_{\hat{\mathbf{y}}_{\mathcal{I}}} f^{\mathcal{N}} \left(\hat{\mathbf{y}}_{\mathcal{I}}; \hat{\mathbf{h}}_{\mathcal{I}}, \frac{E_0}{2} \mathbf{I}_B \right) \sum_{b=1}^B \int_{\hat{\mathbf{y}}_{\mathcal{R}}} \frac{1}{(2\pi \frac{E_0}{2})^{B/2}} \times \quad (24)$$

$$\exp \left(-\frac{\|\hat{\mathbf{y}}_{\mathcal{R}} - \hat{\mathbf{h}}_{\mathcal{R}}\|^2}{2 \frac{E_0}{2}} \right) \frac{E_0}{2} \frac{\partial [g_{\mathcal{R}}(\hat{\mathbf{y}})]_b}{\partial [\hat{\mathbf{y}}_{\mathcal{R}}]_b} d\hat{\mathbf{y}}_{\mathcal{R}} d\hat{\mathbf{y}}_{\mathcal{I}}$$

$$= \frac{E_0}{B} \mathbb{E} \left[\sum_{b=1}^B \frac{\partial [g_{\mathcal{R}}(\hat{\mathbf{y}})]_b}{\partial [\hat{\mathbf{y}}_{\mathcal{R}}]_b} \right], \quad (25)$$

where step (a) follows from integration by parts. Analogously, we have

$$\frac{2}{B} \mathbb{E} \left[g_{\mathcal{I}}(\hat{\mathbf{y}})^T (\hat{\mathbf{y}}_{\mathcal{I}} - \hat{\mathbf{h}}_{\mathcal{I}}) \right] = \frac{E_0}{B} \mathbb{E} \left[\sum_{b=1}^B \left(\frac{\partial [g_{\mathcal{I}}(\hat{\mathbf{y}})]_b}{\partial [\hat{\mathbf{y}}_{\mathcal{I}}]_b} \right) \right]. \quad (26)$$

By remembering that $g(\hat{\mathbf{y}}) = \mu(\hat{\mathbf{y}}) - \hat{\mathbf{y}}$, and replacing (25) and (26) in the original MSE expression in (19), we obtain

$$MSE = \frac{1}{B} \mathbb{E} [\|\mu(\hat{\mathbf{y}}) - \hat{\mathbf{y}}\|_2^2] + \frac{1}{B} \mathbb{E} [\|\hat{\mathbf{y}} - \hat{\mathbf{h}}\|_2^2] \quad (27)$$

$$+ \frac{E_0}{B} \mathbb{E} \left[\sum_{b=1}^B \left(\frac{\partial [\mu_{\mathcal{R}}(\hat{\mathbf{y}})]_b}{\partial [\hat{\mathbf{y}}_{\mathcal{R}}]_b} + \frac{\partial [\mu_{\mathcal{I}}(\hat{\mathbf{y}})]_b}{\partial [\hat{\mathbf{y}}_{\mathcal{I}}]_b} - 2 \right) \right].$$

The second term in the MSE expression above equals E_0 . For the first and the third terms, we omit the expectation operators to arrive at the following SURE expression:

$$SURE = \frac{1}{B} \|\mu(\hat{\mathbf{y}}) - \hat{\mathbf{y}}\|_2^2 + E_0 \quad (28)$$

$$+ \frac{E_0}{B} \sum_{b=1}^B \left(\frac{\partial [\mu_{\mathcal{R}}(\hat{\mathbf{y}})]_b}{\partial [\hat{\mathbf{y}}_{\mathcal{R}}]_b} + \frac{\partial [\mu_{\mathcal{I}}(\hat{\mathbf{y}})]_b}{\partial [\hat{\mathbf{y}}_{\mathcal{I}}]_b} - 2 \right),$$

for which the relationship $\mathbb{E}[SURE] = MSE$ holds.

APPENDIX B PROOF OF COROLLARY 2

In the complex domain, the soft-thresholding function has the following form [45, App. A]:

$$[\eta(\hat{\mathbf{y}}, \tau)]_b = \frac{\hat{y}_b}{|\hat{y}_b|} \max \{ |\hat{y}_b| - \tau, 0 \}, \quad (29)$$

where we define $\hat{y}_b/|\hat{y}_b| = 0$ for $\hat{y}_b = 0$. In order to compute SURE for this shrinkage function, we will first compute its derivative of real and imaginary parts. For $|\hat{y}_b| < \tau$, we have

$$\frac{\partial [\eta_{\mathcal{R}}(\hat{\mathbf{y}}, \tau)]_b}{\partial [\hat{\mathbf{y}}_{\mathcal{R}}]_b} = \frac{\partial [\eta_{\mathcal{I}}(\hat{\mathbf{y}}, \tau)]_b}{\partial [\hat{\mathbf{y}}_{\mathcal{I}}]_b} = 0. \quad (30)$$

For $|\hat{y}_b| > \tau$, we have

$$\begin{aligned} \frac{\partial [\eta_{\mathcal{R}}(\hat{\mathbf{y}}, \tau)]_b}{\partial [\hat{\mathbf{y}}_{\mathcal{R}}]_b} &= \frac{\partial}{\partial [\hat{\mathbf{y}}_{\mathcal{R}}]_b} \left[[\hat{\mathbf{y}}_{\mathcal{R}}]_b - \frac{\tau [\hat{\mathbf{y}}_{\mathcal{R}}]_b}{\sqrt{[\hat{\mathbf{y}}_{\mathcal{R}}]_b^2 + [\hat{\mathbf{y}}_{\mathcal{I}}]_b^2}} \right] \\ &= 1 - \tau \frac{[\hat{\mathbf{y}}_{\mathcal{R}}]_b^2}{([\hat{\mathbf{y}}_{\mathcal{R}}]_b^2 + [\hat{\mathbf{y}}_{\mathcal{I}}]_b^2)^{3/2}} \end{aligned} \quad (31)$$

and

$$\frac{\partial [\eta_{\mathcal{I}}(\hat{\mathbf{y}}, \tau)]_b}{\partial [\hat{\mathbf{y}}_{\mathcal{I}}]_b} = \frac{\partial}{\partial [\hat{\mathbf{y}}_{\mathcal{I}}]_b} \left[[\hat{\mathbf{y}}_{\mathcal{I}}]_b - \frac{\tau [\hat{\mathbf{y}}_{\mathcal{I}}]_b}{\sqrt{[\hat{\mathbf{y}}_{\mathcal{R}}]_b^2 + [\hat{\mathbf{y}}_{\mathcal{I}}]_b^2}} \right]$$

Note that the derivative of $[\eta(\hat{\mathbf{y}}, \tau)]_b$ has a discontinuity at $\tau = |\hat{y}_b|$ (see Figure 3) and thus, SURE is not defined for this value. Using (30), (31) and (32), the complex-valued SURE expression (7) reduces to

$$\begin{aligned} SURE_{\tau} &= \frac{1}{B} \sum_{b=1}^B \min \{ |\hat{y}_b|, \tau \}^2 + E_0 \\ &+ \frac{E_0}{B} \sum_{b: |\hat{y}_b| > \tau} \left(2 - \tau \frac{1}{\sqrt{[\hat{\mathbf{y}}_{\mathcal{R}}]_b^2 + [\hat{\mathbf{y}}_{\mathcal{I}}]_b^2}} - 2 \right) \\ &+ \frac{E_0}{B} \sum_{b: |\hat{y}_b| < \tau} (0 - 2) \end{aligned} \quad (33)$$

$$= \frac{1}{B} \sum_{b: |\hat{y}_b| < \tau} |\hat{y}_b|^2 + \frac{1}{B} \sum_{b: |\hat{y}_b| > \tau} \tau^2 + E_0 \quad (34)$$

APPENDIX C PROOF OF THEOREM 3

We now prove the convergence of SURE in (10). In [54, Lem. 4.14], the authors prove convergence of SURE to MSE in the real domain for the soft-thresholding function. We follow the same procedure for the complex domain. Using [45, Thm. III.15 & III.16], we have that for any pseudo-Lipschitz function $\gamma: \mathbb{C}^2 \rightarrow \mathbb{R}$ the following equality holds:

$$\begin{aligned} \lim_{B \rightarrow \infty} \frac{1}{B} \sum_{b=1}^B \gamma(\eta(\hat{y}_b, \tau), \hat{h}_b) \\ = \mathbb{E} [\gamma(\eta(H + \sqrt{E_0}Z, \tau), H)]. \end{aligned} \quad (35)$$

Here, $Z \sim \mathcal{CN}(0, 1)$ and H is a random variable with the sparse distribution of a channel coefficient in the beamspace domain \hat{h}_b . Using (35), we have the following result

$$\begin{aligned} \lim_{B \rightarrow \infty} \frac{1}{B} \sum_{b=1}^B |\eta(\hat{y}_b, \tau) - \hat{y}_b|^2 \\ = \mathbb{E}_{\hat{y}_b} [|\eta(\hat{y}_b, \tau) - \hat{y}_b|^2], \end{aligned} \quad (36)$$

where, \hat{y}_b is any element of the random vector $\hat{\mathbf{y}}$. The expression above can be rewritten as

$$\lim_{B \rightarrow \infty} \frac{1}{B} \|\eta(\hat{\mathbf{y}}, \tau) - \hat{\mathbf{y}}\|_2^2 = \mathbb{E}_{\hat{\mathbf{y}}} \left[\frac{1}{B} \|\eta(\hat{\mathbf{y}}, \tau) - \hat{\mathbf{y}}\|_2^2 \right]. \quad (37)$$

Now, since $\frac{\partial [\eta_{\mathcal{R}}(\hat{\mathbf{y}}, \tau)]_b}{\partial [\hat{\mathbf{y}}_{\mathcal{R}}]_b} + \frac{\partial [\eta_{\mathcal{I}}(\hat{\mathbf{y}}, \tau)]_b}{\partial [\hat{\mathbf{y}}_{\mathcal{I}}]_b}$ is bounded, it is pseudo-Lipschitz. Hence, we can use (35) to obtain the following convergence result:

$$\begin{aligned} \lim_{B \rightarrow \infty} \frac{1}{B} \sum_{b=1}^B \left(\frac{\partial [\mu_{\mathcal{R}}(\hat{\mathbf{y}})]_b}{\partial [\hat{\mathbf{y}}_{\mathcal{R}}]_b} + \frac{\partial [\mu_{\mathcal{I}}(\hat{\mathbf{y}})]_b}{\partial [\hat{\mathbf{y}}_{\mathcal{I}}]_b} - 2 \right) \\ = \frac{1}{B} \mathbb{E} \left[\sum_{b=1}^B \left(\frac{\partial [\mu_{\mathcal{R}}(\hat{\mathbf{y}})]_b}{\partial [\hat{\mathbf{y}}_{\mathcal{R}}]_b} + \frac{\partial [\mu_{\mathcal{I}}(\hat{\mathbf{y}})]_b}{\partial [\hat{\mathbf{y}}_{\mathcal{I}}]_b} - 2 \right) \right]. \end{aligned} \quad (38)$$

By summing (37) and (38), combined with the fact that $\frac{1}{B} \mathbb{E} [\|\hat{\mathbf{y}} - \hat{\mathbf{h}}\|_2^2] = E_0$, we have established that $\lim_{B \rightarrow \infty} SURE_{\tau} = \mathbb{E}[SURE_{\tau}]$. Finally, using Theorem 1, we also prove that $\lim_{B \rightarrow \infty} SURE_{\tau} = MSE$.

REFERENCES

- [1] R. Ghods, A. Gallyas-Sanhueza, S. H. Mirfarshbafan, and C. Studer, "BEACHES: Beamspace channel estimation for multi-antenna mmWave systems and beyond," in *Proc. IEEE Int. Workshop Signal Process. Advances Wireless Commun. (SPAWC)*, Jul. 2019, pp. 1–5.
- [2] T. S. Rappaport, S. Sun, R. Mayzus, H. Zhao, Y. Azar, K. Wang, G. N. Wong, J. K. Schulz, M. Samimi, and F. Gutierrez, "Millimeter wave mobile communications for 5G cellular: It will work!" *IEEE Access*, vol. 1, pp. 335–349, May 2013.

- [3] A. L. Swindlehurst, E. Ayanoglu, P. Heydari, and F. Capolino, "Millimeter-wave massive MIMO: The next wireless revolution?" *IEEE Commun. Mag.*, vol. 52, no. 9, pp. 56–62, Sep. 2014.
- [4] F. Rusek, D. Persson, B. Kiong, E. G. Larsson, T. L. Marzetta, O. Edfors, and F. Tufvesson, "Scaling up MIMO: Opportunities and challenges with very large large arrays," *IEEE Signal Process. Mag.*, vol. 30, no. 1, pp. 40–60, Jan. 2013.
- [5] E. G. Larsson, F. Tufvesson, O. Edfors, and T. L. Marzetta, "Massive MIMO for next generation wireless systems," *IEEE Commun. Mag.*, vol. 52, no. 2, pp. 186–195, Feb. 2014.
- [6] T. S. Rappaport, G. R. MacCartney, M. K. Samimi, and S. Sun, "Wideband millimeter-wave propagation measurements and channel models for future wireless communication system design," *IEEE Trans. Commun.*, vol. 63, no. 9, pp. 3029–3056, Sep. 2015.
- [7] Z. Gao, C. Hu, L. Dai, and Z. Wang, "Channel estimation for millimeter-wave massive MIMO with hybrid precoding over frequency-selective fading channels," *IEEE Commun. Lett.*, vol. 20, no. 6, pp. 1259–1262, Jun. 2016.
- [8] A. Alkhateeb, G. Leus, and R. W. Heath Jr., "Limited feedback hybrid precoding for multi-user millimeter wave systems," *IEEE Trans. Wireless Commun.*, vol. 14, no. 11, pp. 6481–6494, Nov. 2015.
- [9] F. Sohrabi and W. Yu, "Hybrid digital and analog beamforming design for large-scale antenna arrays," *IEEE J. Sel. Topics Signal Process.*, vol. 10, no. 3, pp. 501–513, Apr. 2016.
- [10] J. Chen, "Hybrid beamforming with discrete phase shifters for millimeter-wave massive MIMO systems," *IEEE Trans. Veh. Technol.*, vol. 66, no. 8, pp. 7604–7608, Aug. 2017.
- [11] S. Dutta, C. N. Barati, A. Dhananjay, D. A. Ramirez, J. F. Buckwalter, and S. Rangan, "A case for digital beamforming at mmWave," *IEEE Trans. Wireless Commun.*, vol. 19, no. 2, pp. 756–770, Feb. 2020.
- [12] P. Skrimponis, S. Dutta, M. Mezzavilla, S. Rangan, S. H. Mirfarshbafan, C. Studer, J. Buckwalter, and M. Rodwell, "Power consumption analysis for mobile mmwave and sub-THz receivers," in *2020 IEEE 6G Wireless Summit*, Mar. 2020, pp. 1–5.
- [13] S. Jacobsson, G. Durisi, M. Coldrey, U. Gustavsson, and C. Studer, "Throughput analysis of massive MIMO uplink with low-resolution ADCs," *IEEE Trans. Wireless Commun.*, vol. 16, no. 6, pp. 4038–4051, Jun. 2017.
- [14] Y. Li, C. Tao, G. Seco-Granados, A. Mezghani, A. L. Swindlehurst, and L. Liu, "Channel estimation and performance analysis of one-bit massive MIMO systems," *IEEE Trans. Signal Process.*, vol. 65, no. 15, pp. 4075–4089, Aug. 2017.
- [15] J. Mo, P. Schniter, and R. W. Heath Jr., "Channel estimation in broadband millimeter wave MIMO systems with few-bit ADCs," *IEEE Trans. Signal Process.*, vol. 66, no. 5, pp. 1141–1154, Mar. 2016.
- [16] T. S. Rappaport, R. W. Heath Jr., R. C. Daniels, and J. N. Murdock, *Millimeter Wave Wireless Communications*. Prentice Hall, 2015.
- [17] A. Alkhateeb, O. El Ayach, G. Leus, and R. W. Heath Jr., "Channel estimation and hybrid precoding for millimeter wave cellular systems," *IEEE J. Sel. Topics Signal Process.*, vol. 8, no. 5, pp. 831–846, Oct. 2014.
- [18] J. Mo, P. Schniter, N. González Prelicic, and R. W. Heath Jr., "Channel estimation in millimeter wave MIMO systems with one-bit quantization," in *Proc. Asilomar Conf. Signals, Syst., Comput.*, Pacific Grove, CA, USA, Nov. 2014, pp. 957–961.
- [19] P. Schniter and A. Sayeed, "Channel estimation and precoder design for millimeter-wave communications: The sparse way," in *Proc. Asilomar Conf. Signals, Syst., Comput.*, Nov. 2014, pp. 273–277.
- [20] J. Deng, O. Tirkkonen, and C. Studer, "mmWave channel estimation via atomic norm minimization for multi-user hybrid precoding," in *Proc. IEEE Wireless Commun. Netw. Conf. (WCNC)*, Apr. 2018, pp. 1–6.
- [21] Y. Wang, P. Xu, and Z. Tian, "Efficient channel estimation for massive MIMO systems via truncated two-dimensional atomic norm minimization," in *Proc. IEEE Int. Conf. Commun. (ICC)*, May 2017, pp. 1–6.
- [22] J. Lee, G. Gil, and Y. H. Lee, "Channel estimation via orthogonal matching pursuit for hybrid MIMO systems in millimeter wave communications," *IEEE Trans. Commun.*, vol. 64, no. 6, pp. 2370–2386, Jun. 2016.
- [23] P. Mächler, "VLSI architectures for compressive sensing and sparse signal recovery," Ph.D. dissertation, ETH Zürich, Switzerland, 2012.
- [24] C. Tsai, Y. Liu, and A. Wu, "Efficient compressive channel estimation for millimeter-wave large-scale antenna systems," *IEEE Trans. Signal Process.*, vol. 66, no. 9, pp. 2414–2428, May 2018.
- [25] J. Brady, N. Behdad, and A. M. Sayeed, "Beamspace MIMO for millimeter-wave communications: System architecture, modeling, analysis, and measurements," *IEEE Trans. Antennas Propag.*, vol. 61, no. 7, pp. 3814–3827, Jul. 2013.
- [26] G. Tang, B. N. Bhaskar, P. Shah, and B. Recht, "Compressed sensing off the grid," *IEEE Trans. Inf. Theory*, vol. 59, no. 11, pp. 7465–7490, Nov. 2013.
- [27] B. N. Bhaskar, G. Tang, and B. Recht, "Atomic norm denoising with applications to line spectral estimation," *IEEE Trans. Signal Process.*, vol. 61, no. 23, pp. 5987–5999, Dec. 2013.
- [28] P. Zhang, L. Gan, S. Sun, and C. Ling, "Atomic norm denoising-based channel estimation for massive multiuser MIMO systems," in *Proc. IEEE Int. Conf. Commun. (ICC)*, Jun. 2015, pp. 4564–4569.
- [29] B. Mamandipoor, D. Ramasamy, and U. Madhow, "Newtonized orthogonal matching pursuit: Frequency estimation over the continuum," *IEEE Trans. Signal Process.*, vol. 64, no. 19, pp. 5066–5081, Oct. 2016.
- [30] F. Bellili, F. Sohrabi, and W. Yu, "Generalized approximate message passing for massive MIMO mmWave channel estimation with Laplacian prior," *IEEE Trans. Commun.*, vol. 67, no. 5, pp. 3205–3219, May 2019.
- [31] C. Huang, L. Liu, C. Yuen, and S. Sun, "Iterative channel estimation using LSE and sparse message passing for mmWave MIMO systems," *IEEE Trans. Signal Process.*, vol. 67, no. 1, pp. 245–259, Jan. 2019.
- [32] C. Jeon, O. Castañeda, and C. Studer, "A 354 Mb/s 0.37 mm² 151 mW 32-user 256-QAM near-MAP soft-input soft-output massive MU-MIMO data detector in 28nm CMOS," *IEEE Solid-State Circuits Lett.*, vol. 2, no. 9, pp. 127–130, Sep. 2019.
- [33] C. Yeh, T. Chu, C. Chen, and C. Yang, "A hardware-scalable DSP architecture for beam selection in mm-Wave MU-MIMO systems," *IEEE Trans. Circuits Syst. I*, vol. 65, no. 11, pp. 3918–3928, Aug. 2018.
- [34] X. Liu, J. Sha, H. Xie, F. Gao, S. Jin, Z. Zhang, X. You, and C. Zhang, "Efficient channel estimator with angle-division multiple access," *IEEE Trans. Circuits Syst. I*, vol. 66, no. 2, pp. 708–718, Sep. 2018.
- [35] L. Somappa, S. Aeron, A. G. Menon, S. Sonkusale, A. A. Seshia, and M. S. Baghini, "On quantized analog compressive sensing methods for efficient resonator frequency estimation," *IEEE Trans. Circuits Syst. I*, pp. 1–10, Jun. 2020.
- [36] M. R. Akdeniz, Y. Liu, M. K. Samimi, S. Sun, S. Rangan, T. S. Rappaport, and E. Erkip, "Millimeter wave channel modeling and cellular capacity evaluation," *IEEE J. Sel. Areas Commun.*, vol. 32, no. 6, pp. 1164–1179, Jun. 2014.
- [37] D. Tse and P. Viswanath, *Fundamentals of Wireless Communication*. Cambridge Univ. Press, 2005.
- [38] C. Studer, M. Wenk, and A. Burg, "MIMO transmission with residual transmit-RF impairments," in *Proc. Int. ITG Workshop on Smart Antennas (WSA)*, Bremen, Germany, Feb. 2010, pp. 189–196.
- [39] A. Gallyas-Sanhueza, S. H. Mirfarshbafan, R. Ghods, and C. Studer, "Sparsity-adaptive beamspace channel estimation for 1-bit mmWave massive MIMO systems," in *IEEE Int. Workshop Signal Process. Advances Wireless Commun. (SPAWC)*, May 2020, to appear.
- [40] S. Jaeckel, L. Raschkowski, K. Börner, L. Thiele, F. Burkhardt, and E. Eberlein, "QuaDRiGa - quasi deterministic radio channel generator user manual and documentation," Fraunhofer Heinrich Hertz Institute, Tech. Rep. v2.0.0, Aug. 2017.
- [41] A. Alkhateeb, O. El Ayach, G. Leus, and R. W. Heath, "Hybrid precoding for millimeter wave cellular systems with partial channel knowledge," in *Proc. Int. Symp. Inf. Theory and its Applicat. (ISITA)*, Feb. 2013, pp. 1–5.
- [42] D. L. Donoho and I. M. Johnstone, "Adapting to unknown smoothness via wavelet shrinkage," *Journal of the American Statistical Association*, vol. 90, no. 432, pp. 1200–1224, Dec. 1995.
- [43] R. Tibshirani, "Regression shrinkage and selection via the lasso," *J. Roy. Statist. Soc. Ser. B*, vol. 58, no. 1, pp. 267–288, Jan. 1996.
- [44] J. A. Tropp and S. J. Wright, "Computational methods for sparse solution of linear inverse problems," *Proceedings of the IEEE*, vol. 98, no. 6, pp. 948–958, Jun. 2010.
- [45] A. Maleki, L. Anitori, Z. Yang, and R. G. Baraniuk, "Asymptotic analysis of complex LASSO via complex approximate message passing (CAMP)," *IEEE Trans. Inf. Theory*, vol. 59, no. 7, pp. 4290–4308, Jul. 2013.
- [46] A. Mousavi, A. Maleki, and R. G. Baraniuk, "Parameterless optimal approximate message passing," Oct. 2013. [Online]. Available: <https://arxiv.org/abs/1311.0035>
- [47] K. Upadhyaya, C. S. Seelamantula, and K. V. S. Hari, "A risk minimization framework for channel estimation in OFDM systems," Oct. 2014. [Online]. Available: <https://arxiv.org/abs/1410.6028>
- [48] C. Studer, S. Fateh, and D. Seethaler, "ASIC implementation of soft-input soft-output MIMO detection using MMSE parallel interference cancellation," *IEEE J. Solid-State Circuits*, vol. 46, no. 7, pp. 1754–1765, Jul. 2011.
- [49] G. H. Golub and C. F. van Loan, *Matrix Computations*, 3rd ed. The Johns Hopkins Univ. Press, 1996.

- [50] D. He, B. Ai, K. Guan, Z. Zhong, B. Hui, J. Kim, H. Chung, and I. Kim, "Channel measurement, simulation, and analysis for high-speed railway communications in 5G millimeter-wave band," *IEEE Trans. Intell. Transp. Syst.*, vol. 19, no. 10, pp. 3144–3158, Oct. 2018.
- [51] P. K. Korrai, K. Deerga Rao, and C. Gangadhar, "FPGA implementation of OFDM-based mmWave indoor sparse channel estimation using OMP," *Springer Circuits, Systems, and Signal Processing*, vol. 37, no. 5, pp. 2194–2205, May 2018.
- [52] S. Birke, W. Chen, G. Wang, D. Auras, C. Shen, R. Leupers, and G. Ascheid, "VLSI implementation of channel estimation for millimeter wave beamforming training," in *IEEE Latin American Symposium on Circuits and Systems (LASCAS)*, Feb. 2018, pp. 1–4.
- [53] K. Li, R. R. Sharan, Y. Chen, T. Goldstein, J. R. Cavallaro, and C. Studer, "Decentralized baseband processing for massive MU-MIMO systems," *IEEE J. Emerging Sel. Topics Circuits Syst.*, vol. 7, no. 4, pp. 491–507, Dec. 2017.
- [54] A. Mousavi, A. Maleki, and R. G. Baraniuk, "Consistent parameter estimation for LASSO and approximate message passing," Nov. 2015. [Online]. Available: <https://arxiv.org/abs/1511.01017>



Seyed Hadi Mirfarshbafan received his B.Sc. and M.Sc. degrees, both in Electrical Engineering from Sharif University of Technology, Tehran, Iran in 2016 and 2018, respectively. In 2020, he received an M.Sc. degree in Electrical and Computer Engineering from Cornell University, Ithaca, NY. He is currently a Ph.D. student in the Integrated Information Processing (IIP) group at ETH Zurich, Zurich, Switzerland. His research interests include wireless communications and design of digital VLSI circuits and systems.



Ramina Ghods is currently a postdoctoral fellow at the Robotics Institute at Carnegie Mellon University working on devising active learning and Bayesian optimization algorithms for active search problems that arise in the fields of robotics. Dr. Ghods received her Ph.D. and M.Sc. degrees in Electrical and Computer Engineering from Cornell University, Ithaca, NY, in 2017 and 2019, respectively. Her thesis focused on the development of novel inference, estimation, and initialization algorithms for applications in machine learning, imaging, and wireless communications. At Cornell, she was the recipient of a 2013–2014 Cornell fellowship and a 2014 Cornell Jacobs Scholar fellowship. Prior to Cornell, she completed her B.Sc. degree in Electrical Engineering from Sharif University of Technology, Tehran, Iran in 2013.



Alexandra Gallyas-Sanhueza is currently a Ph.D. student in the School of Electrical and Computer Engineering at Cornell University, Ithaca, NY. In 2015, she received her B.Sc. degree in Electrical Engineering from Pontificia Universidad Católica de Chile, Santiago, Chile. From 2019 to 2020, she was at Cornell Tech in New York City. Her research interests include signal processing, algorithm design, and wireless communications.



Christoph Studer (S'06, M'10, SM'14) is an Associate Professor at the Department of Information Technology and Electrical Engineering at ETH Zurich, Zurich, Switzerland. In 2009, he received a Ph.D. degree in Information Technology and Electrical Engineering from ETH Zurich. In 2005, he was a Visiting Researcher with the Smart Antennas Research Group at Stanford University. From 2006 to 2009, he was a Research Assistant in both the Integrated Systems Laboratory and the Communication Technology Laboratory (CTL) at ETH Zurich. From 2009 to 2012, Dr. Studer was a Postdoctoral Researcher at CTL, ETH Zurich, and the Digital Signal Processing Group at Rice University. In 2013, he has held the position of Research Scientist at Rice University. From 2014 to 2019, Dr. Studer was an Assistant Professor at Cornell University. From 2019 to 2020, he has been an Associate Professor at Cornell University and at Cornell Tech in New York City. In 2020, he joined ETH Zurich and since 2014, he is also an Adjunct Professor at Rice University.

Dr. Studer's research interests include the design of application-specific integrated circuits, as well as wireless communications, digital signal processing, optimization, and machine learning.

Dr. Studer received ETH Medals for his M.S. and Ph.D. theses in 2006 and 2009, respectively. He received a Swiss National Science Foundation fellowship for Advanced Researchers in 2011 and a US National Science Foundation CAREER Award in 2017. Dr. Studer won a Michael Tien '72 Excellence in Teaching Award from the College of Engineering, Cornell University, in 2016. He shared the Swisscom/ICTnet Innovations Award in both 2010 and 2013. Dr. Studer was the winner of the Student Paper Contest of the 2007 Asilomar Conf. on Signals, Systems, and Computers, received a Best Student Paper Award of the 2008 IEEE Int. Symp. on Circuits and Systems (ISCAS), and shared the best Live Demonstration Award at the IEEE ISCAS in 2013. Dr. Studer is currently an Associate Editor of the IEEE Open Journal of Circuits and Systems (OJCS). In 2019, he was the Technical Program Chair of the Asilomar Conference on Signals, Systems, and Computers, and a Technical Program Co-Chair of the IEEE International Workshop on Signal Processing Systems (SiPS).